Detailed analysis of the three-quark potential in SU(3) lattice QCD

T. T. Takahashi,[1] H. Suganuma,[2] Y. Nemoto,[3] and H. Matsufuru[4]

[1]*RCNP, Osaka University, Mihogaoka 10-1, Ibaraki, Osaka 567-0047, Japan*
[2]*Faculty of Science, Tokyo Institute of Technology, Ohokayama 2-12-1, Meguro, Tokyo 152-8551, Japan*
[3]*Brookhaven National Laboratory, RBRC, Physics Department 510A, Upton, New York 11973-5000*
[4]*YITP, Kyoto University, Kitashirakawa, Sakyo, Kyoto 606-8502, Japan*

The static three-quark (3Q) potential is studied in detail using SU(3) lattice QCD with $12^3 \times 24$ at $\beta = 5.7$ and $16^3 \times 32$ at $\beta = 5.8, 6.0$ at the quenched level. For more than 300 different patterns of the 3Q systems, we perform the accurate measurement of the 3Q Wilson loop with the smearing method, which reduces excited-state contaminations, and present the lattice QCD data of the 3Q ground-state potential V_{3Q}. We perform the detailed fit analysis on V_{3Q} in terms of the *Y Ansatz* both with the continuum Coulomb potential and with the lattice Coulomb potential, and find that the lattice QCD data of the 3Q potential V_{3Q} are well reproduced within a few percent deviation by the sum of a constant, the two-body Coulomb term and the three-body linear confinement term $\sigma_{3Q} L_{\min}$, with $L_{\min}$ the minimal value of the total length of color flux tubes linking the three quarks. From the comparison with the Q-$\bar{\text{Q}}$ potential, we find a universality of the string tension as $\sigma_{3Q} \simeq \sigma_{Q\bar{Q}}$ and the one-gluon-exchange result for the Coulomb coefficients as $A_{3Q} \simeq \frac{1}{2} A_{Q\bar{Q}}$. We investigate also the several fit analyses with the various *Ansätze*: the *Y Ansatz* with the Yukawa potential, the Δ *Ansatz* and a more general *Ansatz* including the *Y* and the Δ *Ansätze* in some limits. All these fit analyses support the *Y Ansatz* on the confinement part in the 3Q potential V_{3Q}, although V_{3Q} seems to be approximated by the Δ *Ansatz* with $\sigma_\Delta \simeq 0.53\sigma$.

I. INTRODUCTION

The strong interaction in hadrons or nuclei is fundamentally ruled by quantum chromodynamics (QCD). In the spirit of the elementary particle physics, it would be desirable to understand hadron physics and nuclear physics at the quark-gluon level based on QCD. However, it still remains a difficult problem to derive even the interquark potential from QCD in the analytic manner, because of the strong-coupling nature of QCD in the infrared region.

In this decade, the lattice QCD calculation has been adopted as a useful and reliable method for the nonperturbative analysis of QCD [1,2]. In particular, the quark-antiquark (Q-$\bar{\text{Q}}$) potential, which is responsible for the meson properties, has been well studied using lattice QCD. The Q-$\bar{\text{Q}}$ potential in lattice QCD is well reproduced by a sum of the Coulomb term due to the perturbative one-gluon-exchange (OGE) process, and the linear confinement term, in addition to an irrelevant constant [3–5]. The linear potential at long distances can be physically interpreted with the flux-tube picture or the string picture for hadrons [6–13] with the string tension $\sigma \simeq 0.89$ GeV/fm, which represents the magnitude of the confinement force. In this picture, the quark and the antiquark are linked with a one-dimensional flux tube with the string tension $\sigma_{Q\bar{Q}}$, and hence the Q-$\bar{\text{Q}}$ potential is proportional to the distance r between the quark and antiquark at the long distance. This flux-tube picture (or the string picture) in the infrared region is supported by the Regge trajectory of hadrons [14,15], the phenomenological analysis of heavy quarkonia data [16], the strong-coupling expansion of QCD [7], and recent lattice QCD simulations [17–19].

However, there is almost no reliable formula to describe the three-quark (3Q) potential V_{3Q} directly based on QCD, other than strong-coupling QCD [7,10], although V_{3Q} is directly responsible for the baryon properties [10,20,21] and is a primary quantity in hadron physics. In fact, the 3Q potential has been treated phenomenologically or hypothetically for more than 20 years. In contrast with a number of studies on the Q-$\bar{\text{Q}}$ potential using lattice QCD [22,23], there were only a few lattice QCD studies for the 3Q potential done mainly more than 14 years ago [24–27].

Even at present, the arguments on the 3Q potential seem to be rather controversial. In Refs. [24,26–29], the 3Q potential seemed to be expressed by a sum of two-body potentials, which supports the Δ-type flux tube picture [30]. On the other hand, Refs. [3,25,31–33] seemed to support the *Y*-type flux-tube picture [10,20] rather than the Δ-type one. These controversial results may be due to the difficulty of the accurate measurement of the 3Q ground-state potential in lattice QCD. For instance, in Refs. [24,26], the authors did not use the smearing for ground-state enhancement, and therefore their results may include serious contamination from the excited-state component. In Refs. [27–29], the author showed a preliminary result only on the equilateral-triangle case without the fit analysis.

In this paper, for more than 300 different patterns of the 3Q system, we perform the accurate measurement of the static 3Q potential in SU(3) lattice QCD at $\beta = 5.7$, 5.8, and 6.0, using the smearing method to remove the excited-state contaminations and to obtain the true ground-state potential. The contents are organized as follows. In Sec. II we make a brief theoretical consideration on the form of the interquark potential based on QCD. In Sec. III we explain the method of

the lattice QCD measurement of the 3Q potential, referring to the importance of the smearing technique and its physical meaning. In Sec. IV we present the lattice QCD data of the 3Q potential, which are accurately measured from the smeared 3Q Wilson loop in a model-independent manner. In Sec. V we perform the fit analysis of the lattice data with the *Y Ansatz*. In Sec. VI we examine the various fit analyses with the Δ *Ansatz* and a more general *Ansatz*, including the *Y* and the Δ *Ansätze* in some limits. Section VII is devoted to the summary and the concluding remarks.

II. THEORETICAL CONSIDERATION ON THE 3Q POTENTIAL

The lattice QCD data themselves are measured in a model-independent way; however, it is useful to make a theoretical consideration on the potential form in the static Q-Q̄ and 3Q systems with respect to QCD. Although QCD is one of the most difficult theories in theoretical particle physics, there are two analytical methods based on QCD: one is the perturbative QCD, which is rather established to describe the short-distance behavior, and the other is the strong-coupling expansion, which is expected to reflect the long-distance behavior of QCD. At the short distance, perturbative QCD would work well according to the asymptotic freedom, and the static interquark potential can be described with the Coulomb-type potential as the one-gluon-exchange (OGE) result. On the other hand, at the long distance at the quenched level, the flux-tube picture with the string tension σ is expected to be applicable from the argument of the strong-coupling expansion of QCD [7,10,20], which indicates a linear-type confinement potential proportional to the total flux-tube length. Of course, it is nontrivial that these simple arguments on ultraviolet and infrared limits of QCD hold for the intermediate region as 0.2 fm<r<1 fm. Nevertheless, for instance, the lattice QCD data of the Q-Q̄ ground-state potential are well fitted by

$$V_{Q\bar{Q}}(r) = -\frac{A_{Q\bar{Q}}}{r} + \sigma_{Q\bar{Q}}r + C_{Q\bar{Q}} \qquad (1)$$

at the quenched level [5]. Also in the phenomenological aspect of QCD, such a Q-Q̄ potential is known to be successful to reproduce the empirical data of the mass spectra and the decay rates of various heavy quarkonia [16]. In fact, the Q-Q̄ potential $V_{Q\bar{Q}}$ is well described by a sum of the short-distance OGE result and the long-distance flux-tube result.

Also for the 3Q ground-state potential V_{3Q}, we basically adopt this picture as a theoretical frame of reference. In the 3Q system in the color-flux-tube picture, reflecting the character of SU(N_c=3) in QCD, there can appear the physical junction linking to the three flux tubes stemming from the valence quarks. Since the confinement part is proportional to the total flux-tube length in this picture, the physical junction is expected to appear at the Fermat point of the 3Q triangle, as shown in Fig. 1, as long as the ground-state 3Q system with spatially fixed valence quarks is concerned. Here, the
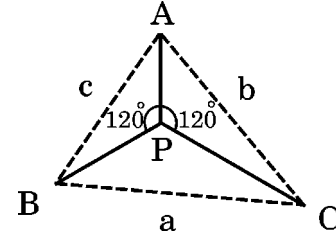

FIG. 1. The flux-tube configuration of the 3Q system with the minimal value of the total flux-tube length. There appears a physical junction linking the three flux tubes at the Fermat point *P*.

Fermat point is defined so as to minimize the sum of the distances to the three vertices of the triangle.

For the convenient description in the argument of the ground-state 3Q potential, we denote by $L_{\min}$ the minimal value of the total length of color flux tubes linking the three quarks. When all angles of the 3Q triangle do not exceed $2\pi/3$, $L_{\min}$ is expressed as

$$L_{\min} = \left[\frac{1}{2}(a^2+b^2+c^2) + \frac{\sqrt{3}}{2} \right.$$

$$\left. \times \sqrt{(a+b+c)(-a+b+c)(a-b+c)(a+b-c)} \right]^{1/2}, \qquad (2)$$

where a, b, and c denote the three sides of the 3Q triangle as shown in Fig. 1. In this case, the physical junction appears and connects the three flux tubes originating from the three quarks, and the shape of the 3Q system is expressed as a *Y*-type flux tube [7,10], where the angle between two flux tubes is found to be $2\pi/3$ [10,20]. When an angle of the 3Q triangle exceeds $2\pi/3$, one finds

$$L_{\min} = a+b+c - \max(a,b,c). \qquad (3)$$

In the picture of the short-distance OGE result plus the long-distance flux-tube result, the 3Q ground-state potential V_{3Q} is expected to take a form of

$$V_{3Q} = -A_{3Q}\sum_{i<j}\frac{1}{|\mathbf{r}_i-\mathbf{r}_j|} + \sigma_{3Q}L_{\min} + C_{3Q}, \qquad (4)$$

which is referred to as the *Y Ansatz* [3,33,20]. In the following sections we will extract first the lattice QCD data of the 3Q potential without any model assumption, and later we will try the fit analysis of the lattice data with the *Y Ansatz* or other possible *Ansätze*.

III. THE LATTICE QCD MEASUREMENT FOR THE 3Q POTENTIAL

A. The 3Q Wilson loop and the 3Q potential in QCD

Similar to the derivation of the Q-Q̄ potential from the Wilson loop, the 3Q static potential V_{3Q} is obtained with the 3Q Wilson loop as
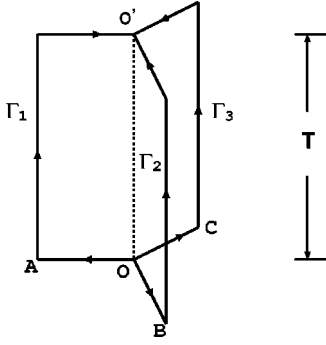
FIG. 2. The 3Q Wilson loop W_{3Q}. The 3Q state is generated at $t=0$ and is annihilated at $t=T$. The three quarks are spatially fixed in $\mathbf{R}^3$ for $0 < t < T$.

$$V_{3Q} = -\lim_{T\to\infty} \frac{1}{T} \ln\langle W_{3Q}\rangle. \tag{5}$$

The 3Q Wilson loop W_{3Q} is defined in a gauge-invariant manner as

$$W_{3Q} \equiv \frac{1}{3!} \varepsilon_{abc} \varepsilon_{a'b'c'} U_1^{aa'} U_2^{bb'} U_3^{cc'} \tag{6}$$

with the path-ordered product

$$U_k \equiv P \exp\left\{ ig \int_{\Gamma_k} dx_\mu A^\mu(x) \right\} \quad (k=1,2,3), \tag{7}$$

along the path denoted by Γ_k in Fig. 2. As shown in Fig. 2, the 3Q Wilson loop physically expresses the 3Q gauge-invariant state which is generated at $t=0$ and is annihilated at $t=T$ with the three quarks spatially fixed in $\mathbf{R}^3$ for $0 < t < T$.

The initial (or the final) 3Q state is introduced as the stringlike object in the naive 3Q Wilson loop. However, the physical ground state of the 3Q system, which is of interest here, is expected to be expressed by the flux tubes instead of the strings, and then the 3Q state which is expressed by the strings generally includes excited-state components such as flux-tube vibrational modes. Of course, if the large T limit can be taken, the ground-state potential would be obtained. However, the practical measurement of $\langle W_{3Q}\rangle$ is rather severe for large T in lattice QCD calculations because $\langle W_{3Q}\rangle$ decreases exponentially with T.

Therefore, for the accurate measurement of the 3Q ground-state potential V_{3Q}, it is practically indispensable to reduce the excited-state components in the 3Q system introduced at $t=0$ and $t=T$ in the 3Q Wilson loop. The gauge-covariant smearing method is one of the most useful techniques for ground-state enhancement [32,34,5] without breaking the gauge covariance, and is adopted to measure the Q-$\bar{\text{Q}}$ potential and the glueball mass [35] in the recent lattice QCD calculation. (This smearing method was not applied to a few pioneering lattice studies on the 3Q potential [24,26], since the smearing technique was mainly developed after their works. As will be discussed later, their numerical results seem to include fatal large excited-state contaminations.)

In this paper we perform the accurate measurement of the 3Q ground-state potential V_{3Q} using the ground-state enhancement by the gauge-covariant smearing method for the link-variable in SU(3)$_c$ lattice QCD at the quenched level [32].

B. The smearing method for the ground-state enhancement

Let us consider here the physical states of the 3Q system with the spatially fixed quarks. In this 3Q system, of course, there is no valence-quark motion, and the central issue is the gluonic configuration under the boundary condition of the spatially fixed three quarks, which play the role of the color source of the gluonic color-electric flux.

Like the Q-$\bar{\text{Q}}$ flux-tube system, the ground state of the 3Q system is expected to be composed by flux tubes rather than the strings [3,12], and there are many excited states of the 3Q system corresponding to the flux-tube vibrational modes [3]. We here express the 3Q Wilson loop with the normalized physical states, the 3Q ground state $|\text{g.s.};t\rangle$, and the kth excited 3Q state $|k\text{th e.s.};t\rangle$ at t. In the 3Q Wilson loop, the normalized gauge-invariant 3Q state $|3Q;0\rangle$ created at $t=0$ and $|3Q;T\rangle$ annihilated at $t=T$ can be expressed as

$$|3Q;0\rangle = c_0|\text{g.s.};0\rangle + c_1|\text{1st e.s.};0\rangle + c_2|\text{2nd e.s.};0\rangle + \cdots,$$

$$|3Q;T\rangle = c_0|\text{g.s.};T\rangle + c_1|\text{1st e.s.};T\rangle + c_2|\text{2nd e.s.};T\rangle + \cdots, \tag{8}$$

with the coefficients c_i obeying the normalization condition $\sum_{i=0}^{\infty}|c_i|^2 = 1$. Then, the expectation value of W_{3Q} can be expressed as

$$\begin{aligned} \langle W_{3Q}(T)\rangle &= \langle 3Q;T|3Q;0\rangle = |c_0|^2 \langle \text{g.s.};T|\text{g.s.};0\rangle \\ &\quad + |c_1|^2 \langle \text{1st e.s.};T|\text{1st e.s.};0\rangle + \cdots \\ &= |c_0|^2 \exp(-V_{\text{g.s.}}T) + |c_1|^2 \exp(-V_{\text{1st e.s.}}T) \\ &\quad + \cdots, \end{aligned} \tag{9}$$

with the ground-state potential $V_{\text{g.s.}}$ and the kth excited-state potential $V_{k\text{th e.s.}}$, which correspond to the energy eigenvalues of the 3Q system. [Note that the normalization here is consistent with the definition of W_{3Q} in Eq. (6), which leads to $\langle W_{3Q}(T=0)\rangle = 1$.]

As increasing T, the excited-state components drop faster than the ground-state component in $\langle W_{3Q}\rangle$; however, the ground-state component $|c_0|^2 \exp(-V_{\text{g.s.}}T)$ also decreases exponentially. Hence, we face a practical difficulty in extracting the numerical signal. To avoid this difficulty, we adopt the smearing technique [3,5,34] which enhances the ground-state overlap as $|c_0|^2$ and removes the excited-state contamination efficiently.

The smearing method is one of the most popular and useful techniques to extract the ground-state potential in lattice QCD. The standard smearing for link variables is expressed as the iterative replacement of the spatial link variable $U_i(s)$ ($i=1,2,3$) by the obscured link variable $\bar{U}_i(s) \in$ SU(3)$_c$ [5,34] which maximizes
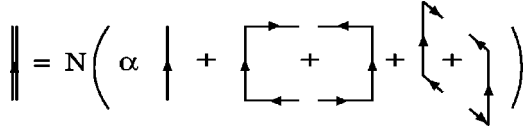
FIG. 3. The schematic explanation of the smearing for the link variables.

$$\operatorname{Re} \operatorname{Tr}\{\bar{U}_i(s)V_i^\dagger(s)\} \qquad (10)$$

with

$$V_i(s) \equiv \alpha U_i(s) + \sum_{j\neq i} \{U_j(s)U_i(s+\hat{j})U_j^\dagger(s+\hat{i})$$

$$+ U_j^\dagger(s-\hat{j})U_i(s-\hat{j})U_j(s+\hat{i}-\hat{j})\}, \qquad (11)$$

which is schematically illustrated in Fig. 3. Here, $\alpha \in \mathbf{R}$ is referred to as the smearing parameter. The nth smeared link variables $U_\mu^{(n)}(s)$ $(n=1,2,\dots,N_{\text{smear}})$ are iteratively defined starting from $U_\mu^{(0)}(s) \equiv U_\mu(s)$ as

$$U_i^{(n)}(s) \equiv \bar{U}_i^{(n-1)}(s) \quad (i=1,2,3), \quad U_4^{(n)}(s) \equiv U_4(s). \qquad (12)$$

For arbitrary operator $F[U_\mu(\cdot)]$, the nth smeared operator $F[U_\mu^{(n)}(\cdot)]$ is defined with the nth smeared link variable $U_\mu^{(n)}(s)$ instead of the original link variable. The interquark potential can be accurately measured from the properly smeared (3Q) Wilson loop. Here, the smearing parameter α and the iteration number n play the role of the variational parameters and are properly chosen so as to maximize the ground-state component.

We note that the smearing is just a method to choose the flux-tube-like operator, and hence it never changes the physics itself such as the gauge configuration. As an important feature, this smearing procedure keeps the gauge covariance of the "fat" link variable $U_\mu^{(n)}(s)$ properly. In fact, the gauge-transformation property of $U_\mu^{(n)}(s)$ is just the same as that of the original link variable $U_\mu(s)$, and therefore the gauge invariance of $F(U_\mu^{(n)}(s))$ is ensured for the arbitrary gauge-invariant operator $F(U_\mu(s))$. For instance, the nth smeared (3Q) Wilson loop is gauge invariant.

While no temporal extension appears in the smearing, the fat link variable $U_\mu^{(n)}(s)$ includes a spatial extension in terms of the original link variable $U_\mu(s)$, and then the smeared "line" expressed with $U_\mu^{(n)}(s)$ physically corresponds to a "flux tube" with the spatial extension. Therefore, if a suitable smearing is done, the smeared line is expected to be close to the ground-state flux tube. This smearing method is actually successful for the extraction of the Q-Q̄ potential in lattice QCD [5].

C. The physical meaning of the smearing method

We consider here the physical meaning of the smearing method with the smearing parameter α in terms of the size or the spatial extension of the nth smeared line. For the convenience of the description, we define
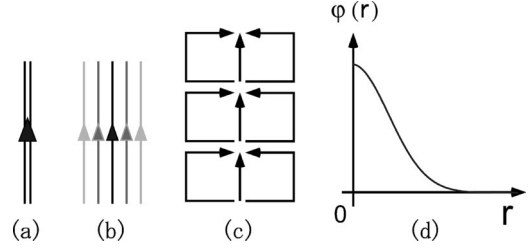

FIG. 4. The schematic explanation of the physical meaning of the smeared line. The nth smeared line depicted as (a) physically corresponds to the spatially-distributed flux tube as (b) in terms of the original field variable. The single smearing procedure for the line is illustrated with (c) on the lattice. The flux perpendicular to the line is expected to be canceled. The spatial distribution of the nth smeared line is expressed by the Gaussian profile $\phi(r)$ with $r = (x^2+y^2)^{1/2}$ as shown in (d).

$$p \equiv \frac{\alpha}{\alpha+4}, \quad q \equiv \frac{1}{\alpha+4}, \qquad (13)$$

which satisfy $p + 4q = 1$. Let us consider the smearing of the linelike object, which is idealized to be infinitely long. As mentioned above, the smeared line corresponds to the spatially extended flux tube in terms of the original link variable. Here, we locate the nth smeared line on the z axis in $\mathbf{R}^3$, and then, due to the translational invariance along the z direction, the argument is essentially two-dimensional and depends only on x and y, and the flux direction is to be in the z direction. We denote by $\varphi(x,y;n)(x,y \in \mathbf{R})$ the spatial flux distribution in the nth smeared line. [On the lattice with the spacing a, $\varphi(x,y;n)$ is defined on the discrete points $(x,y) = (n_x a, n_y a)$ with $n_x, n_y \in \mathbf{Z}$.]

From the iterative definition of the smearing, the spatial flux distribution $\varphi(x,y;n+1)$ of the $(n+1)$th smeared line is expected to relate to $\varphi(x,y;n)$ of the nth smeared line as

$$\varphi(x,y;n+1) = p\varphi(x,y;n) + q\{\varphi(x+a,y;n) + \varphi(x-a,y;n)$$

$$+ \varphi(x,y+a;n) + \varphi(x,y-a;n)\}. \qquad (14)$$

Here, as shown in Fig. 4(c), we assume the cancellation of non-z components of the flux, which exactly holds for the Abelian flux. Using the difference operator, we obtain

$$\Delta_n \varphi(x,y;n) \equiv \varphi(x,y;n+1) - \varphi(x,y;n)$$

$$= q\{\Delta_x \varphi(x,y;n) - \Delta_x \varphi(x-a,y;n)$$

$$+ \Delta_y \varphi(x,y;n) - \Delta_y \varphi(x,y-a;n)\}$$

$$= q\{\Delta_x^B \Delta_x \varphi(x,y;n) + \Delta_y^B \Delta_y \varphi(x,y;n)\}, \qquad (15)$$

where Δ_k and Δ_k^B $(k=x,y)$ denote the forward and the backward difference operators satisfying $\Delta_k f(\vec{r}) \equiv f(\vec{r}+\hat{k}) - f(\vec{r})$ and $\Delta_k^B f(\vec{r}) \equiv f(\vec{r}) - f(\vec{r}-\hat{k})$, respectively.

When the lattice spacing a is small enough, the spatial difference Δ_k can be approximated by the spatial derivative as $\Delta_k \simeq a\partial_k$. Also for the iteration number n of the smearing, we formally introduce a small "spacing" a_n in the "n direction," and we define the semicontinuum parameter $\tilde{n} \equiv na_n$, although the final result does not depend on the ar-

TABLE I. The simulation condition and the related information. For each β, the corresponding lattice spacing a, the lattice size, the number N_{3Q} of the different patterns of the 3Q system analyzed, the number N_{conf} of the gauge configuration used for the measurement, the number N_{therm} of sweeps for the thermalization, the number N_{sep} of sweeps for the separation, the smearing parameter α, the iteration number N_{smr} of the suitable smearing for the 3Q potential, and the used supercomputer are listed.

β	a (fm)	Lattice size	N_{3Q}	N_{conf}	N_{therm}	N_{sep}	α	N_{smr}	Supercomputer
5.7	0.19	$12^3 \times 24$	16	210	5,000	500	2.3	12	NEC SX-4
5.8	0.14	$16^3 \times 32$	139	200	10,000	500	2.3	22	HITACHI SR8000
6.0	0.10	$16^3 \times 32$	155	150	10,000	500	2.3	42	NEC SX-5

tificial spacing a_n. Then, the difference Δ_n can be approximated by the derivative as $\Delta_n \simeq a_n \partial_{\tilde{n}}$. In this way, we obtain the differential equation as

$$\frac{\partial}{\partial \tilde{n}} \varphi(x,y;n) = D(\partial_x^2 + \partial_y^2) \varphi(x,y;n), \qquad (16)$$

which corresponds to the "diffusion equation" at the "time" $\tilde{n}$ with the diffusion parameter

$$D \equiv \frac{qa^2}{a_n} = \frac{1}{\alpha+4} \frac{a^2}{a_n}. \qquad (17)$$

The "initial condition" at $n=0$ is given as

$$\varphi(x,y;n=0) = \delta(x)\delta(y), \qquad (18)$$

which means the simple line before applying the smearing. Then, the flux distribution $\varphi(x,y;n)$ in the nth smeared line can be expressed as

$$\varphi(x,y;n) = \frac{1}{(4\pi D\tilde{n})} \exp\left[-\frac{x^2+y^2}{4D\tilde{n}}\right]. \qquad (19)$$

Thus, the nth smeared line physically corresponds to the Gaussian spatially distributed flux tube in terms of the original link variable as shown in Fig. 4(d).

As a result, the flux-tube size can be roughly estimated as

$$R \equiv \sqrt{\langle x^2+y^2 \rangle} \equiv \left(\frac{\int dxdy\, \varphi(x,y;n)(x^2+y^2)}{\int dxdy\, \varphi(x,y;n)}\right)^{1/2}$$

$$= 2\sqrt{D\tilde{n}} = 2a\sqrt{\frac{n}{\alpha+4}}. \qquad (20)$$

We note that the square root appears as a character of the Brownian motion, and hence the n dependence of the flux-tube radius R is not so strong. This formula also explains the physical roles of the two parameters, α and n. The smearing parameter α controls the speed of the smearing, and the speed of smearing is slower for larger α. For each fixed α, n plays the role of extending the size of the smeared operator. Hence, once we find the suitable smearing param-

eters n and α which achieve a large ground-state overlap, the physical size of the flux tube is roughly estimated with Eq. (20).

IV. THE LATTICE QCD RESULTS OF THE 3Q POTENTIAL

We measure the 3Q potential from the properly smeared 3Q Wilson loop in $SU(3)_c$ lattice QCD at the quenched level. In this section we present the lattice QCD data of the 3Q ground-state potential V_{3Q} for more than 300 different patterns of the 3Q systems in total. These lattice QCD data are, of course, the model-independent data based on QCD, and we think that the data themselves are useful for the study of the 3Q system, particularly for the phenomenological approach as the quark model for baryons.

A. The simulation conditions of lattice QCD

The gauge configurations are generated using the $SU(3)_c$ lattice QCD Monte Carlo simulation with the standard action with $12^3 \times 24$ at $\beta=5.7$ and $16^3 \times 32$ at $\beta=5.8, 6.0$ at the quenched level. The pseudo-heat-bath algorithm is adopted for an update of the gauge configuration. After a thermalization of more than 5000 sweeps, we sample the gauge configuration every 500 sweeps, and we use at least 150 gauge configurations at each β for the study of the 3Q potential. We summarize in Table I the lattice parameters and the related information on the simulation as well as the lattice spacing a determined so as to reproduce the string tension as $\sigma = 0.89$ GeV/fm in the Q-$\bar{Q}$ potential $V_{Q\bar{Q}}$ at each β. As for the smearing, we set the smearing parameter as $\alpha=2.3$, which is one of the most suitable smearing parameters for the calculation of the 3Q ground-state potential. The iteration number N_{smr} of the smearing which maximizes the ground-state overlap is also listed at each β in Table I. (From the numerical test with various smearing parameter sets, we have observed that the smearing with $\alpha=2.3$ and a suitable iteration number N_{smr} listed in Table I provides a large ground-state overlap in the smeared 3Q Wilson loop for $\beta=5.7$, 5.8, and 6.0. This is reflected in the large value of $\bar{C}$ close to unity in Tables II–X.) On the statistical error of the lattice data, we adopt the jackknife error estimate [36]. The Monte Carlo simulations at $\beta=5.7$, 6.0, and 5.8 have been performed on NEC-SX4, NEC-SX5 at Osaka University and HITACHI-SR8000 at KEK, respectively.

TABLE II. Lattice QCD results for the 3Q potential V_{3Q}^{latt} in the lattice unit for 16 patterns of the 3Q system at $\beta=5.7$. (i,j,k) denotes the 3Q system where the three quarks are put on $(i,0,0)$, $(0,j,0)$, and $(0,0,k)$ in $\mathbf{R}^3$ in the lattice unit. For each 3Q configuration, V_{3Q}^{latt} is measured from the single-exponential fit as $\langle W_{3Q}\rangle=\bar{C}e^{-V_{3Q}T}$ in the range of T listed at the fourth column. The statistical errors listed are estimated with the jackknife method, and χ^2/N_{DF} is listed at the fifth column. The best-fit function V_{3Q}^{fit} in the Y Ansatz is added.

(i,j,k)	V_{3Q}^{latt}	$\bar{C}$	Fit range of T	χ^2/N_{DF}	V_{3Q}^{fit}	$V_{3Q}^{\text{latt}}-V_{3Q}^{\text{fit}}$
$(0,1,1)$	0.8457(38)	0.9338(173)	5–10	0.062	0.8524	-0.0067
$(0,1,2)$	1.0973(43)	0.9295(161)	4–8	0.163	1.1025	-0.0052
$(0,1,3)$	1.2929(41)	0.8987(110)	3–7	0.255	1.2929	0.0000
$(0,2,2)$	1.3158(44)	0.9151(120)	3–6	0.053	1.3270	-0.0112
$(0,2,3)$	1.5040(63)	0.9041(170)	3–6	0.123	1.5076	-0.0036
$(0,3,3)$	1.6756(43)	0.8718(73)	2–5	0.572	1.6815	-0.0059
$(1,1,1)$	1.0238(40)	0.9345(149)	4–8	0.369	1.0092	0.0146
$(1,1,2)$	1.2185(62)	0.9067(228)	4–8	0.352	1.2151	0.0034
$(1,1,3)$	1.4161(49)	0.9297(135)	3–7	0.842	1.3964	0.0197
$(1,2,2)$	1.3866(48)	0.9012(127)	3–7	0.215	1.3895	-0.0029
$(1,2,3)$	1.5594(63)	0.8880(165)	3–6	0.068	1.5588	0.0006
$(1,3,3)$	1.7145(43)	0.8553(76)	2–6	0.412	1.7202	-0.0057
$(2,2,2)$	1.5234(37)	0.8925(65)	2–5	0.689	1.5238	-0.0004
$(2,2,3)$	1.6750(118)	0.8627(298)	3–6	0.115	1.6763	-0.0013
$(2,3,3)$	1.8239(56)	0.8443(90)	2–5	0.132	1.8175	0.0064
$(3,3,3)$	1.9607(93)	0.8197(154)	2–5	0.000	1.9442	0.0165

B. The Q-$\bar{\text{Q}}$ potential

As a frame of reference, we measure the Q-$\bar{\text{Q}}$ potential $V_{Q\bar{Q}}$ from the properly smeared Wilson loop in the present lattice QCD. As is consistent with the previous lattice works [5], the lattice QCD data of the Q-$\bar{\text{Q}}$ ground-state potential $V_{Q\bar{Q}}$ at the quenched level are well reproduced by

$$V_{Q\bar{Q}}(r)=-\frac{A_{Q\bar{Q}}}{r}+\sigma_{Q\bar{Q}}r+C_{Q\bar{Q}} \qquad (21)$$

with the best-fit parameter set $(A_{Q\bar{Q}},\ \sigma_{Q\bar{Q}},\ C_{Q\bar{Q}})$ listed in Table XI at each β. As a visual illustration, we show in Fig. 5 the lattice QCD data of $V_{Q\bar{Q}}(r)$ as the function of the interquark distance r in the lattice unit. One finds a good agreement of the lattice data of $V_{Q\bar{Q}}$ and the fit curve with Eq. (21).

In spite of the visual agreement, the statistical analysis is also necessary for the argument on the fit. This is rather difficult because the lattice QCD data include not only the statistical error but also the systematic errors from the discretization, which cannot be estimated straightforwardly. We here examine the on-axis and the off-axis data at each β. The on-axis data of $V_{Q\bar{Q}}$ are well fitted with Eq. (21) at each β. However, when we include the off-axis data, the fit of $V_{Q\bar{Q}}$ with Eq. (21) becomes rather worse as $\chi^2/N_{\text{DF}}\sim 10$. This is due to the breaking of the rotational invariance on the lattice, and such breaking is significant for the short-distance data.

As will be discussed in Sec. V E, to be strict the lattice Coulomb potential would be preferable instead of the Coulomb potential, at least for the short-distance lattice data. We examine also the fit with the lattice Coulomb plus linear potential, and list the best-fit parameter set $(A_{Q\bar{Q}}^{\text{LC}},\ \sigma_{Q\bar{Q}}^{\text{LC}},\ C_{Q\bar{Q}}^{\text{LC}})$ at each β together with χ^2/N_{DF} in Table XI, where the label as "off-axis" means the fit analysis for both on-axis and off-axis data. We then find that the fit with the lattice Coulomb plus linear potential for both on-axis and off-axis data is fairly good, although the fit parameters such as the string tension are almost unchanged.

C. The ground-state enhancement through the smearing

Before presenting the lattice data of the 3Q potential, we briefly demonstrate the utility of the smearing method by estimating the magnitude of the ground-state component in the 3Q state at $t=0,T$ in the smeared 3Q Wilson loop W_{3Q}, which is composed with the nth smeared link variable $U_\mu^{(n)}(s)$.

From the similar argument in the Q-$\bar{\text{Q}}$ system [5], the overlap of the 3Q-state operator with the ground state is estimated with

$$C_0\equiv\frac{\langle W_{3Q}(T)\rangle^{T+1}}{\langle W_{3Q}(T+1)\rangle^T}, \qquad (22)$$

which is referred to as the ground-state overlap. For instance, in the ideal case where the 3Q state is the perfect ground state in the smeared 3Q Wilson loop, one gets $\langle W_{3Q}(T)\rangle=e^{-V_{3Q}T}$ and then $C_0=1$. [Here, $W_{3Q}(T)$ is normalized as $\langle W_{3Q}(T=0)\rangle=1$, as shown in Eq. (6).] In accordance with the excited-state contamination, C_0 is reduced to be a small value less than unity.

TABLE III. A part of lattice QCD results for the 3Q potential V_{3Q}^{latt} at $\beta=5.8$. (i,j,k) denotes the 3Q system where the three quarks are put on $(i,0,0)$, $(0,j,0)$, and $(0,0,k)$ in $\mathbf{R}^3$ in the lattice unit. For each 3Q configuration, V_{3Q}^{latt} is measured from the single-exponential fit as $\langle W_{3Q}\rangle=\bar{C}e^{-V_{3Q}T}$. The prefactor $\bar{C}$ physically means the magnitude of the ground-state component. The difference from the best-fit function V_{3Q}^{fit} in the Y Ansatz is added. The listed values are measured in the lattice unit.

(i,j,k)	V_{3Q}^{latt}	$\bar{C}$	$V_{3Q}^{\text{latt}}-V_{3Q}^{\text{fit}}$
(0,1,1)	0.7697(12)	0.9554(58)	−0.0041
(0,1,2)	0.9639(28)	0.9269(128)	−0.0039
(0,1,3)	1.1112(60)	0.9274(274)	0.0053
(0,1,4)	1.2337(119)	0.9106(538)	0.0064
(0,1,5)	1.3219(235)	0.7957(927)	−0.0195
(0,1,6)	1.4518(132)	0.8583(442)	0.0000
(0,1,7)	1.5719(72)	0.8798(182)	0.0119
(0,1,8)	1.6621(105)	0.8189(261)	−0.0048
(0,2,2)	1.1370(16)	0.9342(46)	−0.0018
(0,2,3)	1.2659(21)	0.9145(52)	−0.0027
(0,2,4)	1.3585(239)	0.7975(946)	−0.0279
(0,2,5)	1.4834(128)	0.8448(431)	−0.0152
(0,2,6)	1.6082(28)	0.8810(50)	0.0004
(0,2,8)	1.8251(132)	0.8548(332)	0.0036
(0,3,3)	1.3925(91)	0.9168(330)	−0.0003
(0,3,4)	1.5005(41)	0.8862(109)	−0.0066
(0,3,5)	1.6130(25)	0.8810(41)	−0.0042
(0,3,6)	1.7171(32)	0.8581(54)	−0.0080
(0,4,4)	1.6077(72)	0.8655(185)	−0.0112
(0,4,5)	1.7163(32)	0.8581(52)	−0.0109
(0,4,6)	1.8262(40)	0.8482(67)	−0.0075
(0,4,7)	1.9321(51)	0.8317(82)	−0.0070
(0,4,8)	2.0413(65)	0.8202(101)	−0.0025
(0,5,5)	1.8193(44)	0.8372(72)	−0.0147
(0,5,6)	1.9282(47)	0.8265(76)	−0.0111
(0,5,8)	2.1460(73)	0.8047(113)	−0.0017
(0,6,6)	2.0322(62)	0.8083(102)	−0.0113
(0,6,7)	2.1401(71)	0.7964(112)	−0.0070
(0,6,8)	2.2384(85)	0.7698(123)	−0.0118
(0,7,7)	2.2461(101)	0.7813(153)	−0.0037
(0,7,8)	2.3390(114)	0.7462(166)	−0.0134
(0,8,8)	2.4191(177)	0.6949(244)	−0.0351
(1,1,1)	0.9140(32)	0.9424(147)	0.0149
(1,1,2)	1.0647(42)	0.9290(194)	0.0096
(1,1,3)	1.1914(86)	0.8917(384)	0.0053
(1,1,4)	1.2879(172)	0.7887(674)	−0.0169
(1,1,5)	1.4201(39)	0.8662(104)	0.0024
(1,1,6)	1.5335(54)	0.8600(136)	0.0061
(1,1,7)	1.6497(36)	0.8686(59)	0.0146
(1,1,8)	1.7557(46)	0.8509(76)	0.0140
(1,2,2)	1.1865(33)	0.9186(120)	0.0020
(1,2,3)	1.3126(124)	0.9411(576)	0.0072
(1,2,4)	1.4155(28)	0.8845(72)	−0.0043
(1,2,5)	1.5248(41)	0.8678(106)	−0.0056

TABLE IV. A part of lattice QCD results for the 3Q potential V_{3Q}^{latt} at $\beta=5.8$. The notations are the same in Table III.

(i,j,k)	V_{3Q}^{latt}	$\bar{C}$	$V_{3Q}^{\text{latt}}-V_{3Q}^{\text{fit}}$
(1,2,6)	1.6356(57)	0.8587(145)	−0.0031
(1,2,7)	1.7490(36)	0.8591(59)	0.0035
(1,2,8)	1.8545(44)	0.8407(70)	0.0032
(1,3,3)	1.4175(33)	0.9020(86)	−0.0024
(1,3,4)	1.5301(109)	0.9083(391)	−0.0005
(1,3,5)	1.6272(50)	0.8538(125)	−0.0116
(1,3,6)	1.7301(72)	0.8285(178)	−0.0154
(1,3,7)	1.8300(105)	0.7978(249)	−0.0213
(1,3,8)	1.9505(50)	0.8196(78)	−0.0057
(1,4,4)	1.6284(60)	0.8652(154)	−0.0099
(1,4,5)	1.7195(73)	0.8133(173)	−0.0251
(1,4,6)	1.8213(90)	0.7883(212)	−0.0286
(1,4,7)	1.9469(47)	0.8216(72)	−0.0075
(1,4,8)	2.0543(59)	0.8078(91)	−0.0043
(1,5,5)	1.8114(119)	0.7692(271)	−0.0378
(1,5,7)	2.0496(55)	0.8048(85)	−0.0071
(1,5,8)	2.1538(67)	0.7863(100)	−0.0063
(1,6,7)	2.1642(71)	0.8056(112)	0.0055
(1,6,8)	2.2632(74)	0.7794(113)	0.0020
(1,7,7)	2.2808(92)	0.8080(147)	0.0203
(1,7,8)	2.3682(96)	0.7642(141)	0.0059
(1,8,8)	2.4512(156)	0.7146(217)	−0.0123
(2,2,2)	1.2771(73)	0.9000(258)	−0.0041
(2,2,3)	1.3783(80)	0.8755(277)	−0.0107
(2,2,4)	1.4899(42)	0.8768(107)	−0.0074
(2,2,5)	1.5933(54)	0.8513(133)	−0.0113
(2,2,8)	1.9188(49)	0.8210(79)	−0.0024
(2,3,3)	1.4739(120)	0.8636(410)	−0.0142
(2,3,4)	1.5831(22)	0.8718(36)	−0.0081
(2,3,5)	1.6820(57)	0.8380(140)	−0.0133
(2,3,6)	1.7915(34)	0.8361(58)	−0.0080
(2,3,7)	1.8982(43)	0.8220(68)	−0.0053
(2,3,8)	2.0002(53)	0.7989(85)	−0.0071
(2,4,4)	1.6805(77)	0.8506(189)	−0.0102
(2,4,5)	1.7675(71)	0.7952(166)	−0.0246
(2,4,7)	1.9863(48)	0.7933(73)	−0.0107
(2,4,8)	2.0982(60)	0.7875(94)	−0.0015
(2,5,8)	2.2004(72)	0.7756(106)	0.0051
(2,6,6)	2.0932(65)	0.7907(94)	0.0016
(2,6,7)	2.1928(71)	0.7665(105)	0.0010
(2,6,8)	2.2889(84)	0.7378(120)	−0.0038
(2,7,8)	2.4014(106)	0.7347(147)	0.0103
(3,3,3)	1.5566(72)	0.8434(180)	−0.0197
(3,3,4)	1.6474(66)	0.8125(160)	−0.0253
(3,3,5)	1.7641(37)	0.8353(60)	−0.0084
(3,3,6)	1.8685(44)	0.8196(72)	−0.0053
(3,3,7)	1.9696(52)	0.7965(82)	−0.0062
(3,3,8)	2.0753(65)	0.7812(98)	−0.0029
(3,4,5)	1.8357(106)	0.7690(240)	−0.0249

TABLE V. A part of lattice QCD results for the 3Q potential V_{3Q}^{latt} at $\beta = 5.8$. The notations are the same in Table III.

(i,j,k)	V_{3Q}^{latt}	$\bar{C}$	$V_{3Q}^{latt} - V_{3Q}^{fit}$
(3,4,6)	1.9440(157)	0.7686(358)	-0.0153
(3,4,7)	2.0569(60)	0.7756(96)	-0.0025
(3,4,8)	2.1666(68)	0.7679(100)	0.0063
(3,5,5)	1.9321(178)	0.7527(394)	-0.0220
(3,5,6)	2.0504(56)	0.7756(83)	-0.0004
(3,5,8)	2.2627(77)	0.7491(110)	0.0138
(3,6,6)	2.1580(69)	0.7683(101)	0.0123
(3,7,7)	2.3578(110)	0.7261(155)	0.0190
(3,7,8)	2.4496(125)	0.6934(169)	0.0133
(3,8,8)	2.5416(178)	0.6613(229)	0.0088
(4,4,4)	1.8377(49)	0.8044(74)	-0.0119
(4,4,5)	1.9371(55)	0.7900(82)	-0.0044
(4,4,6)	2.0367(61)	0.7703(91)	-0.0004
(4,5,5)	2.0278(68)	0.7638(96)	-0.0022
(4,5,6)	2.1301(69)	0.7503(99)	0.0073
(4,6,6)	2.2310(87)	0.7347(123)	0.0174
(4,6,8)	2.4356(117)	0.7003(162)	0.0322
(4,7,7)	2.4304(130)	0.6947(177)	0.0306
(4,7,8)	2.5347(150)	0.6806(201)	0.0402
(4,8,8)	2.6412(245)	0.6696(328)	0.0531
(5,5,5)	2.1192(87)	0.7417(123)	0.0050
(5,5,6)	2.2247(90)	0.7334(125)	0.0208
(5,5,7)	2.3298(104)	0.7208(147)	0.0328
(5,5,8)	2.4280(131)	0.6980(182)	0.0357
(5,6,6)	2.3159(114)	0.7065(155)	0.0252
(5,6,7)	2.4124(125)	0.6818(170)	0.0307
(5,6,8)	2.5255(151)	0.6802(200)	0.0503
(5,8,8)	2.7193(345)	0.6369(438)	0.0660
(6,6,6)	2.4166(223)	0.6943(306)	0.0421
(6,6,7)	2.5096(190)	0.6648(252)	0.0468
(6,6,8)	2.6408(230)	0.6868(315)	0.0866
(6,7,7)	2.5846(264)	0.6148(323)	0.0358
(6,7,8)	2.7365(260)	0.6615(343)	0.0981
(6,8,8)	2.8742(456)	0.6939(633)	0.1479

TABLE VI. A part of lattice QCD results for the 3Q potential V_{3Q}^{latt} at $\beta = 5.8$. (l,m,n) denotes the 3Q system where the three quarks are put on $(l,0,0)$, $(-m,0,0)$, and $(0,n,0)$ in $\mathbf{R}^3$ in the lattice unit. The other notations are the same in Table III.

(l,m,n)	V_{3Q}^{latt}	$\bar{C}$	$V_{3Q}^{latt} - V_{3Q}^{fit}$
(1,2,1)	1.1185(22)	0.9321(80)	0.0199
(1,5,2)	1.5721(55)	0.8586(140)	-0.0052
(1,6,2)	1.6804(76)	0.8446(190)	-0.0030
(1,7,2)	1.7949(40)	0.8514(64)	0.0063
(2,3,2)	1.4653(19)	0.9028(33)	0.0068
(2,4,2)	1.5757(21)	0.8896(32)	0.0125
(2,5,2)	1.6820(30)	0.8708(51)	0.0152
(3,3,2)	1.5732(27)	0.8879(45)	0.0144
(3,4,2)	1.6793(33)	0.8689(52)	0.0203
(3,4,3)	1.7660(36)	0.8592(54)	-0.0035
(3,5,3)	1.8677(43)	0.8377(67)	-0.0002
(4,4,3)	1.8692(48)	0.8449(77)	0.0056

D. The lattice QCD data of the 3Q potential

Now, we perform the accurate measurement of the 3Q ground-state potential V_{3Q} using the smearing technique in SU(3) lattice QCD. We investigate more than 300 different patterns of the 3Q systems in total. In the practical calculation, we consider the following two type 3Q system on the lattice: (I) The 3Q system where the three quarks are put on the three spatial axes as $(i,0,0),(0,j,0),(0,0,k)$ $(i,j,k = 0,1,2,\ldots)$ in $\mathbf{R}^3$ in the lattice unit; (II) the 3Q system where the three quarks are put on the x-y plane as $(l,0,0)$, $(-m,0,0),(0,n,0)$ $(l,m,n = 0,1,2,\ldots)$ in $\mathbf{R}^3$ in the lattice unit.

In both cases, the junction point O in the 3Q Wilson loop is set at the origin $(0,0,0)$ in $\mathbf{R}^3$, although the final result of the ground-state potential V_{3Q} should not depend on the artificial selection of O. [As will be shown in the fit analysis in Sec. V, there is no discontinuity between (I) and (II) on the 3Q potential V_{3Q}, in spite of the fairly different setting of the artificial junction O. This suggests that V_{3Q} is independent of O.] For each pattern of the 3Q system, we calculate the 3Q Wilson loop of all equivalent 3Q systems by changing O and the direction of $\hat{x},\hat{y},\hat{z}$, using the translational, the rotational, and the reflection symmetries on lattices.

Owing to the smearing, the ground-state component is largely enhanced, and therefore the 3Q Wilson loop $\langle W_{3Q} \rangle$ composed with the smeared link variable exhibits a single-exponential behavior as

$$\langle W_{3Q} \rangle \simeq e^{-V_{3Q}T} \tag{23}$$

even for a small value of T.

For each 3Q configuration, we measure V_{3Q}^{latt} from the least-squares fit with the single-exponential form

$$\langle W_{3Q} \rangle = \bar{C} e^{-V_{3Q}T}. \tag{24}$$

Here, we choose the fit range of T such that the stability of the "effective mass"

We note that the ground-state potential V_{3Q} can be measured accurately if C_0 is large enough and is close to unity. Then, we check the ground-state overlap C_0 in the nth smeared 3Q Wilson loop $\langle W_{3Q}(U_\mu^{(n)}(s),T) \rangle$ using lattice QCD simulations, and we search reasonable values of the smearing parameter α and the iteration number N_{smr} of the smearing so as to make C_0 large. For instance, the ground-state overlap C_0 is largely enhanced as $0.8 < C_0 < 1$ even for $T \leq 3$ by the smearing with $\alpha = 2.3$ and $N_{smr} = 12$ for all of the 3Q configurations at $\beta = 5.7$ as shown in Fig. 6. Thus, the ground-state component is largely enhanced by the suitable smearing.

We list in Table I one of the best parameter sets (α, N_{smr}) at each β. We note that, as will be shown in the next section, the magnitude of the ground-state overlap can be also estimated with $\bar{C}$ in Tables II–X. One finds a large value of $\bar{C}$ close to unity as $\bar{C} \gtrsim 0.7$ for each lattice data on the 3Q system.

TABLE VII. A part of lattice QCD results for the 3Q potential V_{3Q}^{latt} at $\beta = 6.0$. (i,j,k) denotes the 3Q system where the three quarks are put on $(i,0,0)$, $(0,j,0)$, and $(0,0,k)$ in $\mathbf{R}^3$ in the lattice unit. For each 3Q configuration, V_{3Q}^{latt} is measured from the single-exponential fit as $\langle W_{3Q} \rangle = \bar{C} e^{-V_{3Q}T}$. The prefactor $\bar{C}$ physically means the magnitude of the ground-state component. The difference from the best-fit function V_{3Q}^{fit} in the Y Ansatz is added. The listed values are measured in the lattice unit.

(i,j,k)	V_{3Q}^{latt}	$\bar{C}$	$V_{3Q}^{\text{latt}} - V_{3Q}^{\text{fit}}$
(0,1,1)	0.6778(6)	0.9784(24)	−0.0012
(0,1,2)	0.8234(11)	0.9712(45)	−0.0042
(0,1,3)	0.9183(17)	0.9769(65)	0.0045
(0,1,4)	0.9859(24)	0.9589(92)	0.0050
(0,1,5)	1.0463(30)	0.9495(112)	0.0064
(0,1,6)	1.1069(40)	0.9595(152)	0.0122
(0,1,7)	1.1572(50)	0.9374(192)	0.0102
(0,2,2)	0.9430(21)	0.9586(78)	−0.0095
(0,2,3)	1.0259(24)	0.9607(91)	−0.0045
(0,2,4)	1.0946(32)	0.9657(120)	0.0003
(0,2,5)	1.1454(41)	0.9282(149)	−0.0064
(0,2,6)	1.2075(28)	0.9464(76)	0.0018
(0,2,7)	1.2563(33)	0.9262(90)	−0.0012
(0,3,3)	1.0999(23)	0.9566(62)	−0.0031
(0,3,4)	1.1595(25)	0.9454(67)	−0.0044
(0,3,5)	1.2170(25)	0.9426(65)	−0.0026
(0,3,6)	1.2699(32)	0.9327(90)	−0.0027
(0,3,7)	1.3216(40)	0.9232(110)	−0.0021
(0,3,8)	1.3765(37)	0.9241(92)	0.0029
(0,4,4)	1.2177(32)	0.9394(87)	−0.0050
(0,4,5)	1.2723(34)	0.9336(96)	−0.0047
(0,4,6)	1.3302(40)	0.9418(110)	0.0013
(0,4,7)	1.3744(42)	0.9128(108)	−0.0048
(0,4,8)	1.4233(51)	0.8982(138)	−0.0054
(0,5,5)	1.3251(40)	0.9265(112)	−0.0050
(0,5,6)	1.3762(39)	0.9187(108)	−0.0049
(0,5,7)	1.4273(49)	0.9110(131)	−0.0035
(0,5,8)	1.4799(51)	0.9079(140)	0.0002
(0,6,6)	1.4248(52)	0.9047(136)	−0.0066
(0,6,7)	1.4785(51)	0.9062(130)	−0.0020
(0,6,8)	1.5300(56)	0.9020(146)	0.0011
(0,7,7)	1.5314(35)	0.9058(59)	0.0023
(0,7,8)	1.5811(41)	0.8971(66)	0.0039
(0,8,8)	1.6325(47)	0.8924(76)	0.0078
(1,1,1)	0.7900(21)	0.9588(98)	0.0073
(1,1,2)	0.8992(25)	0.9707(118)	0.0044
(1,1,3)	0.9800(38)	0.9578(182)	0.0052
(1,1,4)	1.0515(25)	0.9677(99)	0.0115
(1,1,5)	1.1105(36)	0.9578(135)	0.0123
(1,1,6)	1.1645(47)	0.9449(175)	0.0120
(1,1,7)	1.2140(59)	0.9227(209)	0.0095
(1,1,8)	1.2662(72)	0.9146(260)	0.0111
(1,2,2)	0.9796(18)	0.9600(68)	−0.0019
(1,2,3)	1.0555(23)	0.9743(89)	0.0029

TABLE VIII. A part of lattice QCD results for the 3Q potential V_{3Q}^{latt} at $\beta = 6.0$. The notations are the same in Table VII.

(i,j,k)	V_{3Q}^{latt}	$\bar{C}$	$V_{3Q}^{\text{latt}} - V_{3Q}^{\text{fit}}$
(1,2,4)	1.1185(31)	0.9689(119)	0.0043
(1,2,5)	1.1720(39)	0.9458(142)	0.0013
(1,2,6)	1.2283(49)	0.9467(182)	0.0043
(1,2,7)	1.2712(60)	0.9015(208)	−0.0042
(1,2,8)	1.3314(66)	0.9262(243)	0.0058
(1,3,3)	1.1166(34)	0.9582(132)	−0.0013
(1,3,4)	1.1783(35)	0.9659(137)	0.0018
(1,3,5)	1.2299(45)	0.9453(174)	−0.0011
(1,3,6)	1.2877(32)	0.9513(87)	0.0045
(1,3,7)	1.3293(58)	0.9095(210)	−0.0047
(1,3,8)	1.3863(40)	0.9214(103)	0.0027
(1,4,4)	1.2296(29)	0.9442(75)	−0.0030
(1,4,5)	1.2863(29)	0.9484(78)	0.0006
(1,4,6)	1.3326(35)	0.9236(90)	−0.0043
(1,4,7)	1.3864(40)	0.9249(102)	−0.0004
(1,4,8)	1.4401(44)	0.9249(117)	0.0042
(1,5,5)	1.3363(37)	0.9370(99)	−0.0013
(1,5,6)	1.3879(37)	0.9316(99)	0.0001
(1,5,7)	1.4318(44)	0.9039(116)	−0.0053
(1,5,8)	1.4837(47)	0.9001(127)	−0.0020
(1,6,6)	1.4344(52)	0.9115(138)	−0.0029
(1,6,7)	1.4870(55)	0.9115(150)	0.0009
(1,6,8)	1.5370(53)	0.9037(142)	0.0030
(1,7,7)	1.5258(65)	0.8729(165)	−0.0084
(1,7,8)	1.5743(69)	0.8624(168)	−0.0075
(1,8,8)	1.6370(44)	0.8888(69)	0.0080
(2,2,2)	1.0405(34)	0.9669(132)	0.0004
(2,2,3)	1.0963(31)	0.9462(115)	−0.0045
(2,2,4)	1.1579(37)	0.9570(144)	−0.0002
(2,2,5)	1.2108(49)	0.9396(181)	−0.0016
(2,2,6)	1.2676(32)	0.9446(90)	0.0031
(2,2,7)	1.3035(69)	0.8803(246)	−0.0117
(2,2,8)	1.3613(42)	0.9000(112)	−0.0035
(2,3,3)	1.1461(39)	0.9322(147)	−0.0087
(2,3,4)	1.1994(40)	0.9247(149)	−0.0089
(2,3,5)	1.2525(52)	0.9200(188)	−0.0079
(2,3,6)	1.3114(32)	0.9368(85)	0.0002
(2,3,7)	1.3499(71)	0.8852(256)	−0.0110
(2,3,8)	1.4000(79)	0.8775(280)	−0.0099
(2,4,4)	1.2565(28)	0.9443(80)	−0.0027
(2,4,5)	1.3041(34)	0.9274(89)	−0.0053
(2,4,6)	1.3549(36)	0.9207(100)	−0.0041
(2,4,7)	1.4006(37)	0.8990(98)	−0.0072
(2,4,8)	1.4535(49)	0.8980(133)	−0.0026
(2,5,5)	1.3505(42)	0.9129(111)	−0.0077
(2,5,6)	1.4074(42)	0.9272(116)	0.0007
(2,5,7)	1.4520(48)	0.9040(126)	−0.0028
(2,6,6)	1.4515(49)	0.9055(130)	−0.0029
(2,6,7)	1.4920(53)	0.8722(135)	−0.0098

TABLE IX. A part of lattice QCD results for the 3Q potential V_{3Q}^{latt} at $\beta = 6.0$. The notations are the same in Table VII.

(i,j,k)	V_{3Q}^{latt}	$\bar{C}$	$V_{3Q}^{latt} - V_{3Q}^{fit}$
(2,6,8)	1.5528(55)	0.8950(133)	0.0039
(2,7,7)	1.5442(61)	0.8727(163)	−0.0044
(2,7,8)	1.5910(71)	0.8585(177)	−0.0042
(2,8,8)	1.6411(84)	0.8518(213)	−0.0004
(3,3,3)	1.1951(31)	0.9424(86)	−0.0060
(3,3,4)	1.2421(28)	0.9308(77)	−0.0080
(3,3,5)	1.2936(34)	0.9280(93)	−0.0059
(3,3,6)	1.3404(42)	0.9075(111)	−0.0082
(3,3,8)	1.4434(52)	0.8992(141)	−0.0020
(3,4,4)	1.2894(32)	0.9292(79)	−0.0066
(3,4,5)	1.3350(34)	0.9142(88)	−0.0081
(3,4,6)	1.3825(40)	0.9014(103)	−0.0082
(3,4,7)	1.4353(49)	0.9033(131)	−0.0029
(3,4,8)	1.4867(56)	0.8987(145)	0.0011
(3,5,6)	1.4273(42)	0.8929(114)	−0.0075
(3,5,7)	1.4791(53)	0.8931(138)	−0.0023
(3,5,8)	1.5260(50)	0.8770(129)	−0.0020
(3,6,6)	1.4737(61)	0.8812(162)	−0.0064
(3,6,7)	1.5234(51)	0.8769(124)	−0.0024
(3,6,8)	1.5734(61)	0.8709(147)	0.0015
(3,7,7)	1.5655(77)	0.8535(203)	−0.0054
(3,7,8)	1.6177(77)	0.8550(189)	0.0013
(3,8,8)	1.6666(92)	0.8458(222)	0.0054
(4,4,4)	1.3255(46)	0.9047(119)	−0.0126
(4,4,5)	1.3765(41)	0.9116(111)	−0.0061
(4,4,6)	1.4262(49)	0.9088(129)	−0.0021
(4,4,7)	1.4745(60)	0.8985(155)	0.0000
(4,4,8)	1.5243(69)	0.8925(174)	0.0034
(4,5,5)	1.4165(49)	0.8903(132)	−0.0086
(4,5,6)	1.4628(51)	0.8808(124)	−0.0065
(4,5,7)	1.5155(59)	0.8868(155)	0.0012
(4,5,8)	1.5651(63)	0.8786(162)	0.0053
(4,6,6)	1.5198(65)	0.9031(175)	0.0076
(4,6,7)	1.5549(66)	0.8608(163)	−0.0013
(4,6,8)	1.6045(75)	0.8552(188)	0.0036
(5,5,5)	1.4653(75)	0.8984(203)	0.0000
(5,5,6)	1.5074(63)	0.8814(158)	−0.0003
(5,5,7)	1.5452(80)	0.8475(199)	−0.0061
(5,5,8)	1.6008(83)	0.8574(208)	0.0050
(5,6,6)	1.5511(72)	0.8689(181)	0.0026
(5,6,8)	1.6385(81)	0.8343(195)	0.0040
(5,7,7)	1.6354(89)	0.8288(216)	0.0029
(5,7,8)	1.6878(93)	0.8325(219)	0.0127
(6,6,6)	1.5953(108)	0.8605(272)	0.0076
(6,6,7)	1.6328(91)	0.8285(222)	0.0040
(6,6,8)	1.6956(46)	0.8595(67)	0.0244
(6,8,8)	1.7701(138)	0.7972(325)	0.0193
(7,7,8)	1.7666(139)	0.7915(326)	0.0188
(7,8,8)	1.8114(166)	0.7795(376)	0.0243

TABLE X. A part of lattice QCD results for the 3Q potential V_{3Q}^{latt} at $\beta = 6.0$. (l,m,n) denotes the 3Q system where the three quarks are put on $(l,0,0)$, $(-m,0,0)$, and $(0,n,0)$ in $\mathbf{R}^3$ in the lattice unit. The other notations are the same in Table VII.

(l,m,n)	V_{3Q}^{latt}	$\bar{C}$	$V_{3Q}^{latt} - V_{3Q}^{fit}$
(1,2,1)	0.9334(16)	0.9726(64)	0.0098
(1,5,2)	1.2001(26)	0.9529(74)	0.0061
(1,6,2)	1.2467(58)	0.9211(214)	0.0009
(2,3,2)	1.1436(22)	0.9600(61)	0.0053
(2,4,2)	1.2017(26)	0.9555(72)	0.0094
(2,5,2)	1.2543(31)	0.9418(84)	0.0106
(2,6,2)	1.3033(37)	0.9218(105)	0.0097
(2,6,3)	1.3496(44)	0.9202(120)	−0.0007
(3,3,2)	1.2022(27)	0.9537(77)	0.0101
(3,4,2)	1.2563(32)	0.9405(90)	0.0130
(3,4,3)	1.2971(31)	0.9330(86)	−0.0011
(3,5,3)	1.3467(40)	0.9215(108)	0.0006
(4,4,3)	1.3440(44)	0.9147(117)	−0.0008

$$V(T) \equiv \ln \frac{\langle W_{3Q}(T) \rangle}{\langle W_{3Q}(T+1) \rangle} \tag{25}$$

is observed to avoid the effect of the excited-state contamination remaining at the small T region. In fact, we use a relatively large value on T as the fit range for the accurate measurement.

In Table II we list the lattice QCD data V_{3Q}^{latt} of the 3Q ground-state potential at $\beta = 5.7$, together with the prefactor $\bar{C}$ in Eq. (24), the fit range of $T \in [T_{min}, T_{max}]$ and χ^2/N_{DF}. In Tables III–X, we list up the lattice QCD data V_{3Q}^{latt} of the 3Q ground-state potential at $\beta = 5.8, 6.0$, together with the prefactor $\bar{C}$ in Eq. (24). The statistical error of V_{3Q}^{latt} is estimated with the jackknife method. We stress again that these lattice QCD data are the model-independent data based on QCD, and we think that the data themselves are useful for the study of the 3Q system, particularly for the phenomenological approach as the quark model for baryons.

We note that the prefactor $\bar{C}$ physically means the magnitude of the ground-state overlap in the smeared 3Q Wilson loop. In fact, the pure ground-state 3Q system leads to $\bar{C} = 1$, and $1 - \bar{C}$ corresponds to the contribution of the excited-state contamination. We find a large ground-state overlap as $\bar{C} \geq 0.7$ for all 3Q configurations.

From the best smearing parameters, $\alpha = 2.3$ and N_{smr}, the flux-tube radius R can be roughly estimated with Eq. (20) at each β. We then get a rough estimate of the flux-tube radius as $R \simeq 0.52$ fm both at $\beta = 5.7, 5.8$, and 6.0. This flux-tube radius R seems consistent with the typical hadron size, and it cannot be negligible in comparison with the flux-tube length between the junction and the quark in the 3Q systems in consideration. In fact, the 3Q systems listed in Tables II–X are to be regarded as a flux-tube rather than the stringlike object, and hence it is nontrivial whether the strong-coupling QCD can be applicable or not in such 3Q systems. Never-

TABLE XI. The main result on the fit analysis of the lattice QCD data with the *Y Ansatz* at each β. We list the best-fit parameter set (σ, A, C) in the function form as $V_{3Q} = -A_{3Q}\Sigma_{i<j}(1/|\mathbf{r}_i - \mathbf{r}_j|) + \sigma_{3Q}L_{\min} + C_{3Q}$, where $L_{\min}$ denotes the minimal value of the *Y*-type flux-tube length. The label of (Latt. Coul.) means the fit with the lattice Coulomb potential instead of the continuum Coulomb potential. The similar fit on the Q-Q̄ potential is also listed: "on-axis" and "off-axis" mean the fit analysis only for on-axis data and for both on-axis and off-axis data, respectively. The universality of the string tension and the OGE result on the Coulomb coefficient are found as $\sigma_{3Q} \simeq \sigma_{Q\bar{Q}}$ and $A_{3Q} \simeq A_{Q\bar{Q}}$, respectively. The listed values are measured in the lattice unit.

	σ	A	C	χ^2/N_{DF}
(a) $\beta=5.7$ (16 quark configurations)				
$3Q_Y$	0.1524(28)	0.1331(66)	0.9182(213)	3.76
$3Q_Y$ (Latt. Coul.)	0.1556(24)	0.1185(53)	0.8876(179)	1.81
$Q\bar{Q}$ (on-axis)	0.1629(47)	0.2793(116)	0.6203(161)	0.59
$Q\bar{Q}$ (on-axis, Latt. Coul.)	0.1603(48)	0.2627(109)	0.6271(165)	0.51
$Q\bar{Q}$ (off-axis, Latt. Coul.)	0.1611(18)	0.2780(44)	0.6430(63)	3.57
(b) $\beta=5.8$ (139 quark configurations)				
$3Q_Y$	0.1027(6)	0.1230(20)	0.9085(55)	5.03
$3Q_Y$ (Latt. Coul.)	0.1031(6)	0.1141(18)	0.8999(54)	4.29
$Q\bar{Q}$ (on-axis)	0.1079(28)	0.2607(174)	0.6115(197)	0.92
$Q\bar{Q}$ (on-axis, Latt. Coul.)	0.1080(28)	0.2377(159)	0.6074(194)	0.76
$Q\bar{Q}$ (off-axis, Latt. Coul.)	0.1018(11)	0.2795(51)	0.6596(53)	1.28
(c) $\beta=6.0$ (155 quark configurations)				
$3Q_Y$	0.0460(4)	0.1366(11)	0.9599(35)	2.81
$3Q_Y$ (Latt. Coul.)	0.0467(4)	0.1256(10)	0.9467(34)	2.22
$Q\bar{Q}$ (on-axis)	0.0506(7)	0.2768(24)	0.6374(30)	3.56
$Q\bar{Q}$ (on-axis, Latt. Coul.)	0.0500(7)	0.2557(22)	0.6373(30)	1.22
$Q\bar{Q}$ (off-axis, Latt. Coul.)	0.0497(5)	0.2572(15)	0.6389(20)	1.59
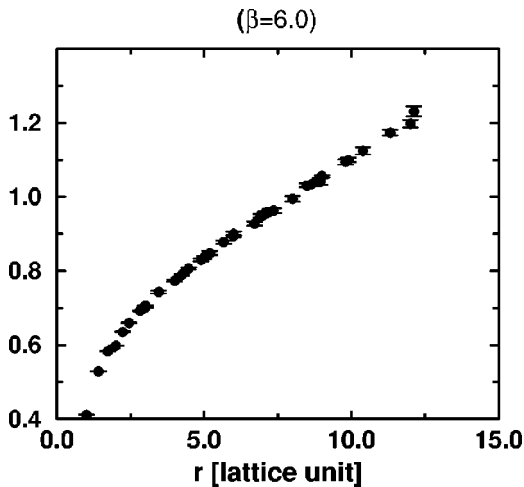
FIG. 5. The Q̄Q̄ static potential $V_{Q\bar{Q}}(r)$ as the function of the interquark distance r in the lattice unit in SU(3) lattice QCD with $\beta=6.0$ at the quenched level.
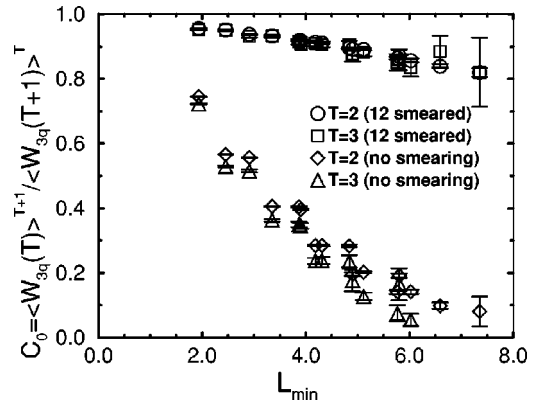
FIG. 6. The ground-state overlap of the 3Q system, $C_0 \equiv \langle W_{3Q}(T)\rangle^{T+1}/\langle W_{3Q}(T+1)\rangle^T$, with the smeared link-variable (upper data) and with the unsmeared link variable (lower data) at $\beta=5.7$. To distinguish the 3Q system, we have taken the horizontal axis as $L_{\min}$, which denotes the minimal value of the total length of the flux tubes linking the three quarks. For each 3Q configuration, C_0 is largely enhanced as $0.8<C_0<1$ by the smearing.
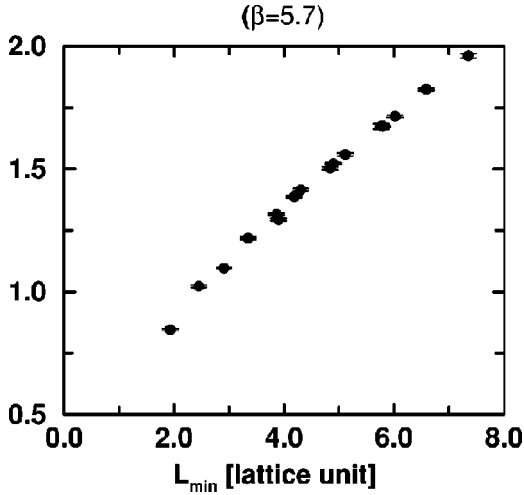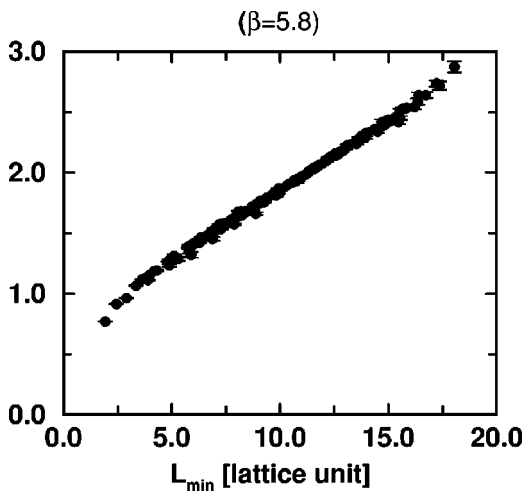
FIG. 7. The lattice QCD data for the 3Q potential V_{3Q}^{latt} at $\beta = 5.7$ as the function of L_{min}, the minimum value of the total length of the flux tubes, in the lattice unit.

theless, the *Y Ansatz* from the simple string picture is found to work well for the lattice QCD data of the three-quark potential.

V. THE FIT ANALYSIS OF THE 3Q POTENTIAL WITH THE *Y ANSATZ*

For the study of the 3Q potential V_{3Q}, we are interested in its large-distance behavior relating to the confinement force rather than the short-distance one. The short-distance behavior of V_{3Q} is expected to be described by the two-body Coulomb potential as the one-gluon-exchange (OGE) result in perturbative QCD, although it is nontrivial whether perturbative QCD works well at the intermediate distance as $r \sim 0.5$ fm. The OGE result indicates also a simple relation on the Coulomb coefficients in the Q-$\bar{Q}$ and the 3Q potentials as $A_{3Q} \simeq \frac{1}{2} A_{Q\bar{Q}}$.

FIG. 8. The lattice QCD data for the 3Q potential V_{3Q}^{latt} at $\beta = 5.8$ as the function of L_{min}, the minimum value of the total length of the flux tubes, in the lattice unit.
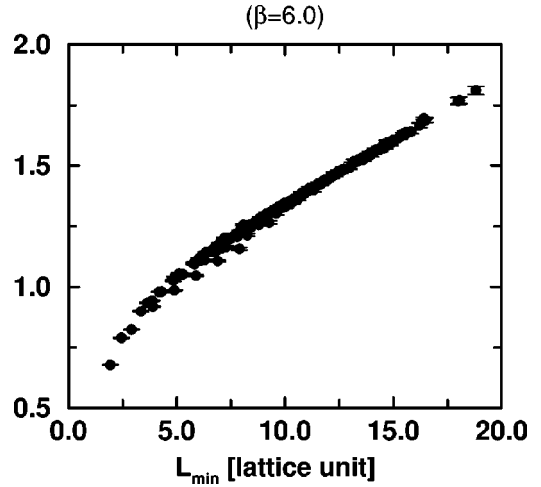
FIG. 9. The lattice QCD data for the 3Q potential V_{3Q}^{latt} at $\beta = 6.0$ as the function of L_{min}, the minimum value of the total length of the flux tubes, in the lattice unit.

A. The long-distance behavior of the 3Q potential

To begin with, we examine the potential form of V_{3Q} at the semiquantitative level. As the Q-$\bar{Q}$ potential, the 3Q potential is also expected to be reproduced by the simple sum of the Coulomb term, the linear confinement term, and a constant. In Figs. 7–9 we plot the 3Q ground-state potential V_{3Q} as the function of the minimal total flux-tube length L_{min}, the minimal value of the total length of color flux tubes linking the three quarks, as discussed in Sec. II. Apart from a constant, V_{3Q} is almost proportional to L_{min} in the infrared region.

To single out the large-distance behavior of V_{3Q} by subtracting perturbative Coulomb contribution, we examine $V_{3Q} - V_{3Q}^{Coul}$. Here, V_{3Q}^{Coul} is defined as
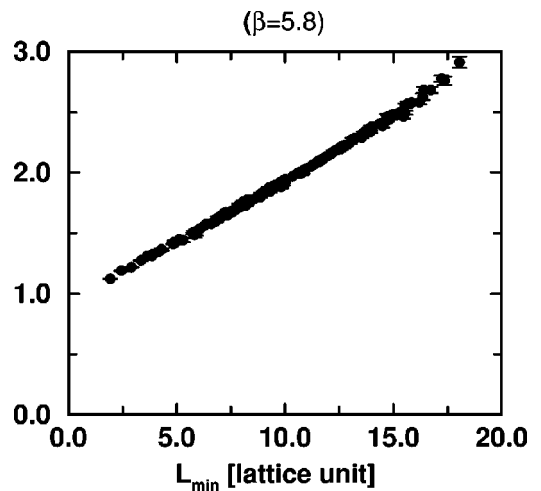

FIG. 10. The semiquantitative test on the confinement part in the 3Q potential V_{3Q} at $\beta = 5.8$. The Coulomb-subtracted potential $V_{3Q}^{latt} - V_{3Q}^{Coul}$ is plotted as the function of L_{min}, the minimal value of the total flux-tube length. Here, the Coulomb part V_{3Q}^{Coul} is evaluated from the Q-$\bar{Q}$ potential.
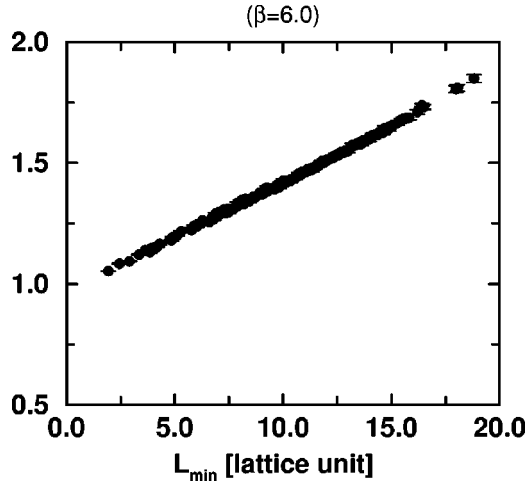
FIG. 11. The semiquantitative test on the confinement part in the 3Q potential V_{3Q} at $\beta=6.0$. The Coulomb-subtracted potential $V_{3Q}^{latt}-V_{3Q}^{Coul}$ is plotted as the function of L_{min}, the minimal value of the total flux-tube length. Here, the Coulomb part V_{3Q}^{Coul} is evaluated from the Q-$\bar{Q}$ potential.

$$V_{3Q}^{Coul}\equiv-\frac{A_{Q\bar{Q}}}{2}\sum_{i<j}\frac{1}{|\mathbf{r}_i-\mathbf{r}_j|}, \qquad (26)$$

which is the potential form expected from the OGE process in perturbative QCD. Reflecting the SU(3) color factor, the coefficient in V_{3Q}^{Coul} between two quarks, of which combination belong the $\bar{3}$ representation, is set to be a half of the coefficient in the color-singlet Q-$\bar{Q}$ system. We note that $A_{Q\bar{Q}}$ is already extracted from the lattice QCD data of the Q-$\bar{Q}$ potential, as shown in Table XI.

In Figs. 10 and 11, we plot $V_{3Q}-V_{3Q}^{Coul}$ as a function of L_{min}, using the lattice data of V_{3Q} and $A_{Q\bar{Q}}$ in Table XI from the Q-$\bar{Q}$ potential. In the whole region, the linearity on L_{min} is observed, which means that the 3Q potential V_{3Q} can be well described by a sum of the perturbative Coulomb term as V_{3Q}^{Coul} and the nonperturbative linear confinement term proportional to L_{min}, as shown in Eq. (4). Thus, the lattice data seem to support the *Y Ansatz*. Note here that this simple fit is not the best fit in terms of the *Y Ansatz* with $(A_{3Q},\sigma_{3Q},C_{3Q})$, and the *Y Ansatz* seems to work well even in this nonbest fit. In the next section, we perform the fit analysis of the 3Q potential with the *Y Ansatz* at the quantitative level.

B. The fit analysis with the *Y Ansatz*

We perform the best-fit analysis for the lattice QCD data of V_{3Q} in terms of the *Y Ansatz* with $(A_{3Q},\sigma_{3Q},C_{3Q})$ at each β. We show in Table XI the best-fit parameter set $(A_{3Q},\sigma_{3Q},C_{3Q})$ in the *Y Ansatz* for V_{3Q} at each β. In Tables II–X, we compare the lattice data V_{3Q}^{latt} with the *Y Ansatz* fitting function V_{3Q}^{fit} in Eq. (4) with the best-fit parameters in Table XI. We observe a good agreement between V_{3Q}^{latt} and V_{3Q}^{fit}. In fact, the deviation $V_{3Q}^{latt}-V_{3Q}^{fit}$ is only within a few percent of the typical scale of V_{3Q} for every lattice data in Tables II–X. (Since the potential includes an irrelevant con-
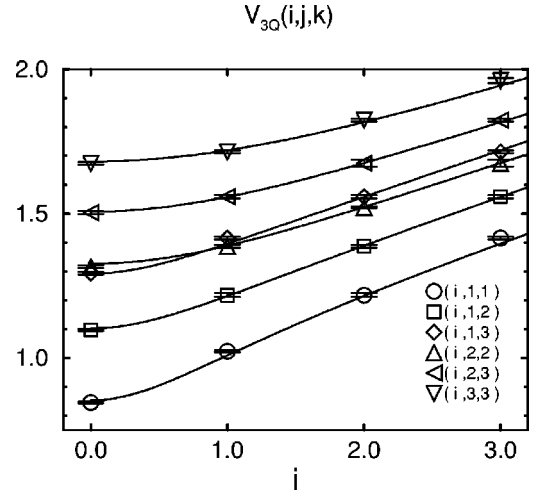

FIG. 12. The comparison between the lattice QCD data V_{3Q}^{latt} at $\beta=5.7$ and the fitted curve of V_{3Q}^{fit} as the function of i for each (j,k) fixed, when the three quarks are located at $(i,0,0),(0,j,0),(0,0,k)$ in the lattice unit. The lattice data V_{3Q}^{latt} are expressed as the points, and V_{3Q}^{fit} is expressed as the solid curve for each (j,k).

stant, the typical scale of V_{3Q} is to be understood as its typical variation among the different 3Q systems rather than the value itself.) Thus, the three-quark ground-state potential V_{3Q} is well described by Eq. (4) of the *Y Ansatz* within a few percent deviation.

As a visual demonstration on the agreement of this fit, we compare in Fig. 12 the lattice QCD data V_{3Q}^{latt} at $\beta=5.7$ and the best-fit curve of V_{3Q}^{fit} as the function of i for each (j,k) fixed, when the three quarks are located at $(i,0,0),(0,j,0),(0,0,k)$ in the lattice unit. While the lattice data V_{3Q}^{latt} are restricted on the integer of i and are expressed as the points, V_{3Q}^{fit} in Eq. (4) can be calculated for an arbitrary real number of i and is expressed as a curve for each (j,k). In Fig. 12 at $\beta=5.7$, one finds a good agreement of the lattice QCD data V_{3Q}^{latt} and the fit curve V_{3Q}^{fit} for each (j,k).

In spite of the good agreement of V_{3Q}^{latt} with V_{3Q}^{fit}, to be strict, χ^2/N_{DF} listed in Table XI seems relatively large, which means the relatively large deviation $V_{3Q}^{latt}-V_{3Q}^{fit}$ in comparison with the error. In addition to physical reasons, this may be due to the underestimate of the error. In fact, the statistical error itself seems very small, but the error should be inevitably enlarged by the systematic error such as the discretization error in lattice calculations. In particular, the statistical error for the short-distance data is rather small, and such a smallness of the short-distance error seems to provide the large value of χ^2/N_{DF}, which may indicate an importance to control the finite lattice-spacing effect. Of course, this point would be clarified if the lattice QCD study with the finer and larger lattice is performed. Besides the direct check on the β dependence, the similar fit analysis with the lattice Coulomb potential is expected to be meaningful. On the lattice, to be strict, the Coulomb potential is to be modified into the lattice Coulomb potential, which contains the finite lattice-spacing effect more directly. Hence, the fit with the lattice Coulomb potential is expected to reduce the discretization error from the finite lattice spacing, especially for the

short-distance data. In Sec. V E, we will perform the fit analysis using the lattice Coulomb potential.

Finally, we compare the best-fit parameter set $(\sigma_{3Q}, A_{3Q}, C_{3Q})$ in the 3Q potential V_{3Q} in Eq. (4) with $(\sigma_{Q\bar{Q}}, A_{Q\bar{Q}}, C_{Q\bar{Q}})$ in the Q-$\bar{Q}$ potential $V_{Q\bar{Q}}$ in Eq. (21) as listed in Table XI. As a remarkable fact, we find a universal feature of the string tension,

$$\sigma_{3Q} \simeq \sigma_{Q\bar{Q}}, \tag{27}$$

as well as the OGE result for the Coulomb coefficient,

$$A_{3Q} \simeq \frac{1}{2} A_{Q\bar{Q}}. \tag{28}$$

C. The model-independent check in the diquark limit

As a model-independent check, we consider the diquark limit, where two quark locations coincide in the 3Q system. In the diquark limit, the static 3Q system becomes equivalent to the Q-$\bar{Q}$ system, which leads to a physical requirement on the relation between V_{3Q} and $V_{Q\bar{Q}}$. Our results, $\sigma_{3Q} \simeq \sigma_{Q\bar{Q}}$ and $A_{3Q} \simeq \frac{1}{2} A_{Q\bar{Q}}$, are consistent with the physical requirement in the diquark limit.

Next, we consider the constant terms C_{3Q} in the diquark limit, although such a constant term is a lattice artifact and is physically irrelevant. As a caution in the continuum diquark limit, there appears a singularity or a divergence from the Coulomb term in V_{3Q} as

$$\lim_{\mathbf{r}_j \to \mathbf{r}_i} \frac{-A_{3Q}}{|\mathbf{r}_i - \mathbf{r}_j|} = -\infty. \tag{29}$$

In the lattice regularization, this ultraviolet divergence is regularized to be a finite constant with the lattice spacing a as

$$\frac{-A_{3Q}}{|\mathbf{r}_i - \mathbf{r}_j|} \to \frac{-A_{3Q}}{\omega a}, \tag{30}$$

where ω is a dimensionless constant satisfying $0 < \omega < 1$ and $\omega \sim 1$. Then, we find

$$C_{3Q} + \frac{-A_{3Q}}{\omega a} = C_{Q\bar{Q}}, \tag{31}$$

or equivalently,

$$C_{3Q} - C_{Q\bar{Q}} = \frac{A_{3Q}}{\omega a} \quad (>0) \tag{32}$$

in the diquark limit. This is the requirement for the constant term in the diquark limit on the lattice. Our lattice QCD results for C_{3Q}, $C_{Q\bar{Q}}$, and A_{3Q} are thus consistent with this requirement, and one finds $\omega \simeq 0.41 - 0.45$: $\omega(\beta=5.7) \simeq 0.447$, $\omega(\beta=5.8) \simeq 0.414$, $\omega(\beta=6.0) \simeq 0.424$.

D. The *Y Ansatz* with the Yukawa potential

In the previous section we adopt the Coulomb potential as the short-distance ingredient, because the OGE process is expected to be dominant at the short distance and the Q-$\bar{Q}$ potential seems to be reproduced with the Coulomb plus linear potential in the lattice QCD. The first reason is, however, nontrivial in the intermediate and the infrared regions, where the perturbative QCD would not work. In fact, due to some nonperturbative effects besides the confinement potential, the Coulomb potential caused by the OGE process may be modified in the infrared region.

For instance, the dual superconductor theory for the quark confinement [12,13,37,38] supports the Yukawa plus linear potential rather than the Coulomb plus linear potential, although the dual gluon mass m_B appearing in the exponent in the Yukawa potential may not be so large, e.g., $m_B \sim 0.5$ GeV both in the model framework [12,13] and in the lattice study [39,40].

From a theoretical viewpoint, such a possibility on the infrared screening of the Coulomb potential seems rather attractive in terms of the empirical absence of the color van der Waals force in the infrared limit [41]. In fact, if the two-body Coulomb potential is not screened in the infrared limit, the color van der Waals force inevitably appears as a long-distance force between hadrons, which is not observed experimentally.

Then, we also investigate the fit analysis of V_{3Q} with the *Y Ansatz* with the Yukawa potential as

$$V_{3Q}^{\text{Yukawa}} \equiv -A_{3Q}^{\text{Yukawa}} \sum_{i<j} V^{\text{Yukawa}}(|\mathbf{r}_i - \mathbf{r}_j|)$$
$$+ \sigma_{3Q}^{\text{Yukawa}} L_{\min} + C_{3Q}^{\text{Yukawa}}, \tag{33}$$

where $V^{\text{Yukawa}}(r)$ denotes the normalized Yukawa potential

$$V^{\text{Yukawa}}(r) \equiv \frac{1}{r} e^{-m_B r}. \tag{34}$$

Here, m_B corresponds to the dual gluon mass in the dual superconductor picture [6,12,13].

We find that the best-fit analysis of the lattice QCD data V_{3Q}^{latt} with V_{3Q}^{Yukawa} indicates $m_B \simeq 0$. Of course, in this special case of $m_B \simeq 0$, the Yukawa potential reduces the Coulomb potential, and the result almost coincides with that in the previous fit. Thus, through the fit analysis with the Yukawa potential based on the *Y Ansatz*, we have observed no definite evidence to replace the Coulomb-potential part by the Yukawa potential in the present calculation.

E. The *Y Ansatz* with the lattice Coulomb potential

So far, we have investigated the fit analysis of the 3Q potential V_{3Q} mainly with the continuum Coulomb and the confinement potential. However, in comparing with the lattice data, the careful treatment considering the lattice discretization effect may be desired. The main effect of the lattice discretization appears only at the short distance, and hence no modification would be necessary for the confine-
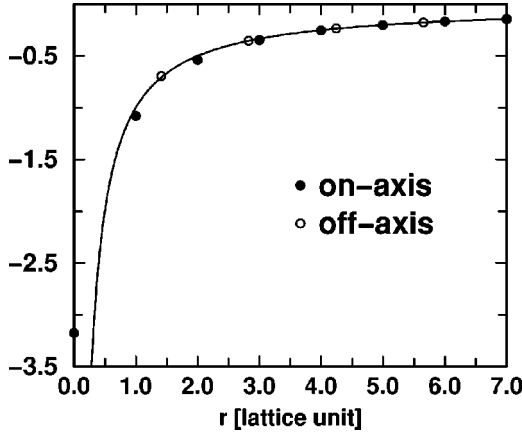
FIG. 13. The comparison of the lattice Coulomb (LC) potential $V^{LC}(\vec{n})$ with $1/r$ in the lattice unit. We plot the on-axis data $V^{LC}(k,0,0)$ $(0 \leq k \leq 7)$ by the closed circle, the off-axis data $V^{LC}(k,k,0)$ $(1 \leq k \leq 4)$ by the open circle, and $1/r$ by the solid curve.

ment potential, which becomes significant only at the large distance. On the other hand, it is nontrivial to use the continuum Coulomb potential for the fit of the lattice data, especially at the short distance, according to the lattice discretization. For instance, the short-distance singularity of the Coulomb potential becomes rather smeared on the lattice, as will be shown later.

In this section we perform the fit analysis of the lattice QCD data of V_{3Q} in terms of the Y Ansatz with the lattice Coulomb potential. The lattice Coulomb (LC) potential between two color charges is obtained with the lattice Coulomb propagator as

$$V^{LC}(\vec{n}) \equiv \pi \int_{-\pi/a}^{\pi/a} \frac{d^3 q}{(2\pi)^3} \frac{\exp(-i\vec{p} \cdot \vec{n}a)}{\sum_{i=1}^{3} \sin^2(p_i a/2)}, \qquad (35)$$

where $\vec{n} \equiv (n_1, n_2, n_3) \in \mathbf{Z}^3$ denotes the relative vector between the two color charges in the lattice unit. Here, the lattice Coulomb potential $V^{LC}(\vec{n})$ is properly normalized so as to reduce into the $1/r$ potential in the continuum limit as

$$V^{LC}(\vec{n}) \rightarrow \frac{1}{r} \qquad (36)$$

with $r = |\vec{n}|a$.

In Fig. 13 we plot $V^{LC}(\vec{n})$ as a function of $|\vec{n}|$ together with $1/r$ as a function of r. One finds that the singularity near the origin $|\vec{n}| = 0$ becomes smeared, and V_{LC} takes a finite value even at $\vec{n} = \vec{0}$, which was mentioned in the context of the diquark limit in the preceding subsection. This may cause a significant deviation in the fit analysis with the $1/r$ Coulomb potential, especially for the short-distance data analysis.

To begin with, we examine the fit analysis of the lattice QCD data on the Q-$\bar{\text{Q}}$ potential $V_{Q\bar{Q}}$ with

$$V_{Q\bar{Q}}^{LC} \equiv -A_{Q\bar{Q}}^{LC} V^{LC}(\vec{n}) + \sigma_{Q\bar{Q}}^{LC} |\vec{n}| + C_{Q\bar{Q}}^{LC}, \qquad (37)$$

using the lattice Coulomb potential $V^{LC}(\vec{n})$. We refer to this fit as the LC fit. We list in Table XI the best-fit parameter set $(A_{Q\bar{Q}}^{LC}, \sigma_{Q\bar{Q}}^{LC}, C_{Q\bar{Q}}^{LC})$ at each β. In Table XI the label "on-axis" means the fit analysis for the on-axis data only, and the label "off-axis" means the fit analysis for both on-axis and off-axis data. In the LC fit, a significant reduction of χ^2/N_{DF} is observed, in comparison with the fit with the $1/r$ Coulomb potential in Eq. (21), as shown in Table XI, in spite of the similar values of the fit parameters. We find a further good agreement between the lattice QCD data and the fitted values of $V_{Q\bar{Q}}^{LC}$ on the Q-$\bar{\text{Q}}$ potential. In particular, the LC fit shows an acceptable value of χ^2/N_{DF} even for the fit on both on-axis and off-axis data, while the fit with the $1/r$ Coulomb potential shows the extremely large χ^2/N_{DF} about 10 when the off-axis data are included. Thus, the discretization effect, which may not be negligible for short-distance data, seems to be taken into account neatly by the use of the LC potential to some extent. Accordingly, the fit analysis with the lattice Coulomb potential V^{LC} seems to provide a more precise information also for the linear confinement potential, although the string tension obtained from the fit analysis is almost unchanged as $\sigma_{Q\bar{Q}}^{LC} \simeq \sigma_{Q\bar{Q}}$.

Now, we perform the LC fit analysis of the lattice data on the 3Q potential V_{3Q} with

$$V_{3Q}^{LC} \equiv -A_{3Q}^{LC} \sum_{i<j} V^{LC}(\vec{n}_{ij}) + \sigma_{3Q}^{LC} L_{min} + C_{3Q}^{LC}, \qquad (38)$$

using the lattice Coulomb potential $V^{LC}(\vec{n})$. In Table XI we list the best-fit parameter set $(A_{3Q}^{LC}, \sigma_{3Q}^{LC}, C_{3Q}^{LC})$ together with the best-fit parameters $(A_{Q\bar{Q}}^{LC}, \sigma_{Q\bar{Q}}^{LC}, C_{Q\bar{Q}}^{LC})$. In this LC fit, χ^2/N_{DF} is reduced in comparison with the fit with the $1/r$ Coulomb potential at each β, as shown in Table XI. Then, this fit seems to be acceptably good even without taking account of the remaining systematic error. Accordingly, the 3Q potential data are well reproduced with the Y Ansatz fit function V_{3Q}^{LC} in Eq. (38) with the lattice Coulomb potential with accuracy better than 1%. Again, the fit analysis with the lattice Coulomb potential V^{LC} is expected to control the discretization effect to some extent, and would provide a more precise information also for the linear confinement potential.

Finally, we focus on the best-fit parameter set $(\sigma_{3Q}^{LC}, A_{3Q}^{LC}, C_{3Q}^{LC})$ in the Y Ansatz with the lattice Coulomb potential. The values of the best-fit parameters in the LC fit are almost the same as those in the previous fit with the $1/r$ Coulomb potential as

$$(\sigma_{3Q}^{LC}, A_{3Q}^{LC}, C_{3Q}^{LC}) \simeq (\sigma_{3Q}, A_{3Q}, C_{3Q}). \qquad (39)$$

In particular, the string tension obtained from the fit analysis is almost unchanged as $\sigma_{3Q}^{LC} \simeq \sigma_{3Q}$. We then find again the universality of the string tension as $\sigma_{3Q}^{LC} \simeq \sigma_{Q\bar{Q}}^{LC}$ at each β. The OGE relation on the Coulomb coefficient is found as $A_{3Q}^{LC} \simeq \frac{1}{2} A_{Q\bar{Q}}^{LC}$. In particular, this OGE relation seems to be ob-

TABLE XII. The fit analysis of the lattice QCD data V_{3Q}^{latt} with the Δ *Ansatz* at each β. We list the best-fit parameter set $(\sigma_\Delta, A_\Delta, C_\Delta)$ in the function form as $-A_\Delta \Sigma_{i<j}(1/|\mathbf{r}_i - \mathbf{r}_j|) + \sigma_\Delta \Sigma_{i<j}|\mathbf{r}_i - \mathbf{r}_j| + C_\Delta$. The label of (Latt. Coul.) means the fit with the lattice Coulomb potential instead of the continuum Coulomb potential. The listed values are measured in the lattice unit.

	β	σ_Δ	A_Δ	C_Δ	χ^2/N_{DF}
$3Q_\Delta$	5.7	0.0858(16)	0.1410(64)	0.9334(210)	10.1
$3Q_\Delta$ (Latt. Coul.)		0.0868(14)	0.1296(51)	0.9146(173)	5.12
$3Q_\Delta$	5.8	0.0581(4)	0.1197(19)	0.8964(55)	13.7
$3Q_\Delta$ (Latt. Coul.)		0.0583(3)	0.1110(18)	0.8872(54)	13.6
$3Q_\Delta$	6.0	0.0264(2)	0.1334(11)	0.9490(36)	3.74
$3Q_\Delta$ (Latt. Coul.)		0.0268(2)	0.1227(10)	0.9361(34)	2.89

served precisely at $\beta=6.0$, which is the finest and the most reliable lattice in the present calculation. (At $\beta=5.7, 5.8$, the ratio $A_{3Q}^{LC}/A_{Q\bar{Q}}^{LC}$ is about 0.4, which seems slightly different from $\frac{1}{2}$ as the OGE result. Note that, however, the discretization error on the QCD action still remains at the small β even with the lattice Coulomb potential. In addition, at $\beta = 5.7, 5.8$, the nearest site is relatively far, and hence the Coulomb contribution to the 3Q potential is relatively small, which may lead to an uncertainty of the Coulomb coefficient.)

To summarize this section, we conclude that the lattice QCD data of the 3Q potential V_{3Q} can be fairly described with the *Y Ansatz* within a few percent deviation, and therefore the nonperturbative linear confinement potential is proportional to L_{min}, the minimal value of the total length of the *Y*-type flux tube linking the three quarks, which supports the *Y Ansatz*.

VI. COMPARISON WITH THE DELTA *ANSATZ* AND THE GENERALIZED *Y ANSATZ*

A. Comparison with the Δ *Ansatz*

For the 3Q potential, the Δ *Ansatz* is also an interesting candidate [30] as well as the *Y Ansatz*. The Δ *Ansatz* is expressed as

$$V_{3Q} = -A_\Delta \sum_{i<j} \frac{1}{|\mathbf{r}_i - \mathbf{r}_j|} + \sigma_\Delta \sum_{i<j} |\mathbf{r}_i - \mathbf{r}_j| + C_\Delta, \quad (40)$$

which consists of the two-body linear potential between quarks. This Δ *Ansatz* has been adopted in a simple nonrelativistic quark potential model [42] because of its simplicity for the calculation. In addition, several lattice QCD studies for the 3Q potential supported the Δ *Ansatz* [24,26–29]. However, Refs. [24,26] seem rather old, done 14 years ago, and were done without smearing, so that the excited-state potential may largely contribute in their measurements. (See Fig. 6.) In a recent paper, Ref. [29], in spite of the use of the smearing, the authors simply compared the 3Q potential V_{3Q} with the *Y* and the Δ *Ansätze* with a fixed string tension estimated from the Q-$\bar{Q}$ potential, only for several equilateral-triangle 3Q configurations without the quantitative fit analysis. Furthermore, in Refs. [27,29], the "deviation" between the lattice data and the *Y Ansatz* seems to be

explained as a trivial constant shift of the potential. In fact, the potential calculated in lattice QCD includes a physically irrelevant constant, which is not properly scaled in the physical unit, as shown in Table XI. If such an irrelevant constant is properly removed, the *Y Ansatz* seems to be better than Δ *Ansatz* even in Refs. [27–29], e.g., the slope of the lattice data V_{3Q}^{latt} seems closer to the *Y Ansatz* rather than the Δ *Ansatz*. In Ref. [29], the authors set the potential origin at the nearest lattice point and used the continuum Coulomb potential for the fit function, but this seems dangerous because a constant deviation may appear as a mismatch between the lattice Coulomb potential which is preferable to the lattice data and the continuum Coulomb potential for the fit function, as shown in Fig. 13. In any case, the quantitative fit analysis is essential for the study of the functional form of the 3Q potential.

In this section we perform the fit analysis with the Δ *Ansatz*. To begin with, we try to fit V_{3Q}^{latt} with the Δ *Ansatz* in Eq. (40), which was suggested in Refs. [24,26,30]. We list in Table XII the best-fit parameter set $(A_\Delta, \sigma_\Delta, C_\Delta)$ in the Δ *Ansatz* at each β. In comparison with the *Y Ansatz*, this fit with the Δ *Ansatz* seems rather worse because of the larger value of χ^2/N_{DF}. In fact, χ^2/N_{DF} is unacceptably large as $\chi^2/N_{DF}=10.1$ at $\beta=5.7$, $\chi^2/N_{DF}=13.7$ at $\beta=5.8$ even for the best fit. (Of course, when σ_Δ is fixed to be the half value of the string tension in the Q-$\bar{Q}$ potential as in Refs. [26–29], this fit with the Δ *Ansatz* becomes further worse with a larger χ^2/N_{DF}.)

As an approximation, however, V_{3Q} seems described by a simple sum of the effective two-body Q-Q potential with a reduced string tension as

$$\sigma_\Delta \simeq 0.53 \sigma_{Q\bar{Q}}. \quad (41)$$

This reduction factor can be naturally understood as a geometrical factor rather than the color factor, since the ratio between L_{min} and the perimeter length L_P of the 3Q triangle satisfies

$$\frac{1}{2} \leqslant \frac{L_{min}}{L_P} \leqslant \frac{1}{\sqrt{3}}, \quad (42)$$

which leads to $L_{min}\sigma = L_P \sigma_{QQ}$ with $\sigma_{QQ}=(0.5\sim 0.58)\sigma$. The OGE relation is also found as $A_\Delta \simeq \frac{1}{2}A_{Q\bar{Q}}$.
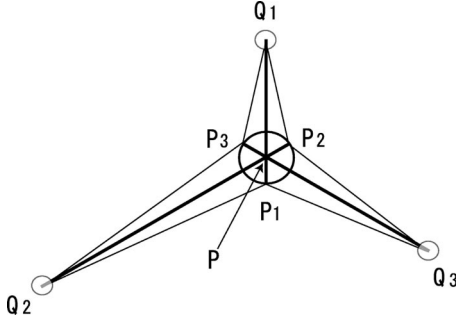
FIG. 14. The visual illustration of the generalized *Y Ansatz*. The three quarks are spatially fixed at Q_1, Q_2, and Q_3. The circle around the Fermat point P corresponds to the flux-tube core around the physical junction. The point P_1 is taken inside the circle so as to minimize $P_1Q_2 + P_1Q_3$, and P_2 and P_3 are similarly defined.

For the fair comparison, we also examine the fit analysis by the Δ *Ansatz* with the lattice Coulomb potential, as was done for the *Y Ansatz* in Sec. V E. The 3Q data are fitted by the form of

$$V_{3Q} = -A_\Delta^{\mathrm{LC}} \sum_{i<j} V^{\mathrm{LC}}(\vec{n}_{ij}) + \sigma_\Delta^{\mathrm{LC}} \sum_{i<j} |\mathbf{r}_i - \mathbf{r}_j| + C_\Delta^{\mathrm{LC}}. \quad (43)$$

We add the results in Table XII. Again, a reduction in χ^2/N_{DF} is observed. The values of the best-fit parameters are almost unchanged, and hence Eq. (41) and the OGE relation also hold. However, in comparison with the *Y Ansatz* with the lattice Coulomb potential, χ^2/N_{DF} in this fit with the Δ *Ansatz* is still larger, and therefore the Δ *Ansatz* is difficult to be accepted.

B. A more general *Ansatz*—the generalized *Y Ansatz*

From the theoretical reason of the short-distance perturbative QCD and the large-distance strong-coupling QCD, the *Y Ansatz* seems reasonable in the both limits. The overall lattice QCD data for the 3Q potential also support the *Y Ansatz* rather than the Δ *Ansatz*. However, it is not trivial whether the *Y Ansatz* holds in the intermediate region as 0.2 fm$<r_{ij}<$0.8 fm. In fact, as was conjectured by Cornwall [30], there is a possibility of the Δ *Ansatz* contamination in this region, where strong-coupling QCD is not applicable. In addition, a few recent lattice works seem to support the Δ *Ansatz* for the 3Q potential in the intermediate region, although their studies were performed only for the equilateral triangle 3Q configuration. Of course, it is rather difficult to analyze the short distance behavior of the non-Coulomb part of the 3Q potential because the Coulomb part is dominant

there. Furthermore, the Coulomb potential form itself is no longer trivial in the intermediate region as 0.2 fm$<r_{ij}<$0.8 fm, where the perturbative QCD would not be valid.

In this section we investigate the lattice QCD data for the 3Q potential using a more general *Ansatz* which includes both the Y and the Δ *Ansätze* in some limits. On the adoption of the general *Ansatz*, we consider the possibility of the flux-tube core effect. For instance, in the dual superconductor picture [12,13,37,38], the hadron flux tube has an intrinsic structure of the core region inside. In fact, if there exists the flux-tube core with the cylindrical radius R_{core}, the Y-type flux tube may be almost identical to the Δ-type configuration at the short distance as $r_{ij} \sim R_{\mathrm{core}}$, and thus the flux-tube length becomes obscured there.

So far, we have defined the minimal flux-tube length, which is proportional to the linear potential, as

$$L_{\mathrm{min}} \equiv PQ_1 + PQ_2 + PQ_3 \quad (44)$$

with the Fermat point P in Fig. 14. In this section, considering a possible flux-tube core effect, we introduce the modified minimal flux-tube length $\overline{L}_{\mathrm{min}}$ defined as

$$\overline{L_{\mathrm{min}}} \equiv \frac{1}{2}(\overline{Q_1P_2Q_3} + \overline{Q_2P_3Q_1} + \overline{Q_3P_1Q_2}), \quad (45)$$

with $\overline{ABC} \equiv \overline{AB} + \overline{BC}$, as shown in Fig. 14. Here, the points P_k ($k=1,2,3$) are taken inside the circle centered at the Fermat point P with the radius R_{core}, and P_1 is chosen so as to minimize

$$\overline{Q_3P_1Q_2} \equiv \overline{P_1Q_2} + \overline{P_1Q_3} \quad (46)$$

and so on. In this definition, when the circle crosses or includes the line Q_2Q_3, P_1 can be taken on the line Q_2Q_3 and then one finds

$$\overline{Q_3P_1Q_2} = \overline{Q_2Q_3}. \quad (47)$$

It is worth mentioning that there are two special cases corresponding to the Y and the Δ *Ansätze*:

$$\overline{L_{\mathrm{min}}} = L_{\mathrm{min}} \quad (48)$$

in the case of $R_{\mathrm{core}}=0$ or $R_{\mathrm{core}} \ll r_{ij}$, and

$$\overline{L_{\mathrm{min}}} = \frac{1}{2}(\overline{Q_1Q_2} + \overline{Q_2Q_3} + \overline{Q_3Q_1}) \quad (49)$$

TABLE XIII. The fit analysis of the lattice QCD data V_{3Q}^{latt} with the generalized *Y Ansatz* at each β. We list the best-fit parameter set $(\sigma_{\mathrm{GY}}, A_{\mathrm{GY}}, C_{\mathrm{GY}}, R_{\mathrm{core}})$ in the lattice unit at $\beta=5.8$ and 6.0. The flux-tube core radius R_{core} in the physical unit is added.

β	σ_{GY}	A_{GY}	C_{GY}	$R_{\mathrm{core}}\,[a]$	R_{core} (fm)	χ^2/N_{DF}
5.8	0.1054(6)	0.1354(18)	0.9569(53)	0.57	0.08	2.63
6.0	0.0480(4)	0.1451(11)	0.9837(33)	0.79	0.08	1.23

in the limit of $R_{core} = \infty$ or $R_{core} \gg r_{ij}$.

Using this modified minimal flux-tube length $\overline{L_{min}}$, we define the generalized *Y Ansatz* as

$$V_{3Q} = \sigma_{GY} \overline{L_{min}} - A_{GY} \sum_{i<j} \frac{1}{|\mathbf{r}_i - \mathbf{r}_j|} + C_{GY}. \qquad (50)$$

This generalized *Y Ansatz* includes both the *Y* and the Δ *Ansätze* in the special cases of $R_{core} = 0$ and $R_{core} = \infty$, respectively. In fact, the generalized *Y Ansatz* reproduces the *Y Ansatz* at the large distance, which is theoretically supported by strong-coupling QCD, with including the Δ *Ansatz* behavior at the short distance.

Then, we investigate the fit analysis for the lattice QCD data of the 3Q potential using the generalized *Y Ansatz* with varying R_{core}. We show in Table XIII the result of the fit analysis at $\beta = 5.8$ and 6.0. We observe the best fitting at $R_{core} \simeq 0.08$ fm both at $\beta = 5.8$ and 6.0. The values of the best-fit parameters ($\sigma_{GY}, A_{GY}, C_{GY}$) are almost the same as those in the *Y Ansatz*. This result also seems to support the *Y Ansatz* rather than the Δ *Ansatz* at the hadronic scale as $r \gg 0.1$ fm. (As an interesting speculation, $R_{core} \simeq 0.08$ fm, which is almost the same both at $\beta = 5.8$ and 6.0, may physically correspond to the flux-tube core radius in the dual superconductor picture.)

VII. SUMMARY AND CONCLUDING REMARKS

We have studied the static three-quark (3Q) potential in detail using SU(3) lattice QCD with $12^3 \times 24$ at $\beta = 5.7$ and $16^3 \times 32$ at $\beta = 5.8, 6.0$ at the quenched level. In the first half of this paper, we have performed accurate measurement of the 3Q Wilson loop with the smearing technique, which reduces excited-state contaminations, and have presented the lattice QCD data of the 3Q ground-state potential V_{3Q} for more than 300 different patterns of the 3Q systems.

In the latter half, we have investigated the fit analysis on

V_{3Q}, and have found that the lattice QCD data of the 3Q potential V_{3Q} are well reproduced within a few percent deviation by the sum of a constant, the two-body Coulomb term, and the three-body linear confinement term $\sigma_{3Q} L_{min}$, with L_{min} the minimal value of the total length of color flux tubes linking the three quarks. We have investigated also the fit analysis with the lattice Coulomb potential instead of the Coulomb potential, and have found a better fit with keeping the similar result. From the comparison with the Q-$\bar{Q}$ potential, we have found a universality of the string tension as $\sigma_{3Q} \simeq \sigma_{Q\bar{Q}}$ and the one-gluon-exchange result for the Coulomb coefficients as $A_{3Q} \simeq \frac{1}{2} A_{Q\bar{Q}}$.

We have also performed the various fit analyses. Through the fit with the Yukawa potential based on the *Y Ansatz*, we have observed no definite evidence that the short-distance potential becomes the Yukawa potential. The fit with the Δ *Ansatz* is worse than that with the *Y Ansatz* on the confinement part in the 3Q potential V_{3Q}, although V_{3Q} seems to be approximated by the Δ *Ansatz* with $\sigma_\Delta \simeq 0.53\sigma$. We have considered a more general *Ansatz* including the *Y* and the Δ *Ansätze* in some limits, and have found a possibility that the *Y*-type flux tube has a flux-tube core about 0.08 fm, which may appear as a small mixing of the Δ *Ansatz* at the short distance, although such a small Δ-type contamination is negligible in the intermediate and the infrared regions. To conclude, all of these detailed fit analyses for the lattice QCD data of the 3Q potential support the *Y Ansatz*.

[1] M. Creutz, *Quarks, Gluons and Lattices* (Cambridge University Press, Cambridge, England, 1983), p. 1.

[2] H. J. Rothe, *Lattice Gauge Theories* (World Scientific, Singapore, 1992), p. 1.

[3] T. T. Takahashi, H. Matsufuru, Y. Nemoto, and H. Suganuma, Phys. Rev. Lett. **86**, 18 (2001).

[4] H. Matsufuru, Y. Nemoto, H. Suganuma, T. T. Takahashi, and T. Umeda, Nucl. Phys. B (Proc. Suppl.) **94**, 554 (2001).

[5] G. S. Bali, C. Schlichter, and K. Schilling, Phys. Rev. D **51**, 5165 (1995).

[6] Y. Nambu, Phys. Rev. D **10**, 4262 (1974).

[7] J. Kogut and L. Susskind, Phys. Rev. D **11**, 395 (1975).

[8] A. Casher, H. Neuberger, and S. Nussinov, Phys. Rev. D **20**, 179 (1979).

[9] J. Carlson, J. B. Kogut, and V. R. Pandharipande, Phys. Rev. D **27**, 233 (1983); **28**, 2807 (1983).

[10] S. Capstick and N. Isgur, Phys. Rev. D **34**, 2809 (1986).

[11] N. Isgur and J. Paton, Phys. Lett. **124B**, 247 (1983); Phys. Rev. D **31**, 2910 (1985).

[12] H. Suganuma, S. Sasaki, and H. Toki, Nucl. Phys. **B435**, 207 (1995).

[13] H. Suganuma, S. Sasaki, H. Toki, and H. Ichie, Prog. Theor. Phys. Suppl. **120**, 57 (1995).

[14] W. Greiner and A. Schäfer, *Quantum Chromodynamics* (Springer, Berlin, 1994), p. 1.

[15] K. Sailer, Th. Schonfeld, Zs. Schram, A. Schafer, and W. Greiner, J. Phys. G **17**, 1005 (1991), and references therein.

[16] W. Lucha, F. F. Schöberl, and D. Gromes, Phys. Rep. **200**, 127 (1991).

[17] A. Di Giacomo, M. Maggiore, and S. Olejnik, Phys. Lett. B **236**, 199 (1990); Nucl. Phys. **B347**, 441 (1990).

[18] Y.-C. Peng and R. W. Haymaker, Phys. Rev. D **47**, 5104 (1993).

[19] R. W. Haymaker, V. Singh, Y.-C. Peng, and J. Wosiek, Phys. Rev. D **53**, 389 (1996).

[20] N. Brambilla, G. M. Prosperi, and A. Vairo, Phys. Lett. B **362**, 113 (1995).

[21] M. Fable de la Ripelle and Yu. A. Simonov, Ann. Phys. (N.Y.) **212**, 235 (1991).

[22] G. S. Bali and K. Schilling, Phys. Rev. D **46**, 2636 (1992).

[23] K. Schilling, Nucl. Phys. B (Proc. Suppl.) **83-84**, 140 (2000) and references therein.

[24] R. Sommer and J. Wosiek, Phys. Lett. **149B**, 497 (1984); Nucl. Phys. **B267**, 531 (1986).

[25] J. Kamesberger, G. Eder, M. E. Faber, H. Leeb, and H. Markum, in *Few-Body Problems in Particle, Nuclear, Atomic, and Molecular Physics*, Proceedings of the XIth European Conference on Few-Body Physics, Fontevraud, 1987, edited by J.-L. Ballot and M. Fabre de la Ripelle (Springer-Verlag, Vienna, 1987), p. 529.

[26] H. B. Thacker, E. Eichten, and J. C. Sexton, Nucl. Phys. B (Proc. Suppl.) **4**, 234 (1988).

[27] G. S. Bali, Phys. Rep. **343**, 1 (2001).

[28] C. Alexandrou, Ph. de Forcrand, and A. Tsapalis, Nucl. Phys. B (Proc. Suppl.) **106**, 403 (2002).

[29] C. Alexandrou, Ph. de Forcrand, and A. Tsapalis, Phys. Rev. D **65**, 054503 (2002).

[30] J. M. Cornwall, Phys. Rev. D **54**, 6527 (1996).

[31] T. T. Takahashi, H. Matsufuru, Y. Nemoto, and H. Suganuma, in *Proceedings of the International Symposium on Dynamics of Gauge Fields*, Tokyo, 1999, edited by A. Chodos, N. Kitazawa, H. Minakata, and C. M. Sommerfield (Universal Academy Press, Tokyo, 2000), p. 179.

[32] H. Suganuma, H. Matsufuru, Y. Nemoto, and T. T. Takahashi, Nucl. Phys. **A680**, 159 (2000).

[33] T. T. Takahashi, H. Suganuma, H. Matsufuru, and Y. Nemoto, in *Proceedings of International Symposium on Hadrons and Nuclei*, Seoul, Korea, 2001, edited by I.-T. Cheon, T. K. Choi, S.-W. Hong, and S. H. Lee, AIP Conf. Proc. No. 594 (AIP, Melville, NY, 2001), p. 341.

[34] APE Collaboration, M. Albanese *et al.*, Phys. Lett. B **192**, 163 (1987).

[35] N. Ishii, H. Suganuma, and H. Matsufuru, hep-lat/0109011; Nucl. Phys. B (Proc. Suppl.) **106**, 516 (2002).

[36] I. Montvay and G. Münster, *Quantum Fields on a Lattice* (Cambridge University Press, Cambridge, England, 1994), p. 389.

[37] *Color Confinement and Hadrons*, edited by H. Toki, Y. Mizuno, H. Suganuma, T. Suzuki, and O. Miyamura (World Scientific, Singapore, 1995), p. 1.

[38] *Quantum Chromodynamics and Color Confinement*, edited by H. Suganuma, M. Fukushima, and H. Toki (World Scientific, Singapore, 2001), p. 1.

[39] H. Suganuma, K. Amemiya, H. Ichie, and A. Tanaka, Nucl. Phys. **A670**, 40 (2000).

[40] H. Suganuma, H. Ichie, A. Tanaka, and K. Amemiya, Prog. Theor. Phys. Suppl. **131**, 559 (1998).

[41] G. Feinberg and J. Sucher, Phys. Rev. D **20**, 1717 (1979).

[42] M. Oka and K. Yazaki, Prog. Theor. Phys. **66**, 556 (1981); **66**, 572 (1981).